Batteries and Supercapacitors

CrossMark

Electrochemical in situ X-ray probing in lithium-ion and sodium-ion batteries

Guobin Zhang[1], Tengfei Xiong[1], Liang He[1], Mengyu Yan[1], Kangning Zhao[1], Xu Xu[1,*], and Liqiang Mai[1,*]

[1] State Key Laboratory of Advanced Technology for Materials Synthesis and Processing, Wuhan University of Technology, Wuhan 430070, China

ABSTRACT

In situ X-ray diffraction (XRD), as a widely used tool in probing the structure evolution in electrochemical process as well as the energy storage and capacity fading mechanism, has shown great effects with optimizing and building better batteries. Based on the research progresses of in situ XRD in recent years, we give a review of the development and the utilization of this powerful tool in understanding the complex electrochemical mechanisms. The studies on in situ XRD are divided into three sections based on the reaction mechanisms: alloying, conversion, and intercalation reactions in lithium-ion batteries. The alloying reaction, in which lithium ions insert into Si, Sb, and Ge is firstly reviewed, followed by a discussion about the recent development of in situ XRD on conversion reaction materials (including metal oxides and metal sulfides) and intercalation reaction materials (including cathode materials and some structure-stable anode materials). As for sodium-ion batteries, we divide these researches on structure evolution into two categories: cathode and anode materials. Finally, the future development of in situ XRD is discussed.

Introduction

With the development of human society, there is an increasing desire for energy storage devices, which will be extensively used in the transportation and the power grid [1–4]. These devices should feature high power density, high energy density as well as long cycling life. Among them, lithium-ion battery (LIB) is techn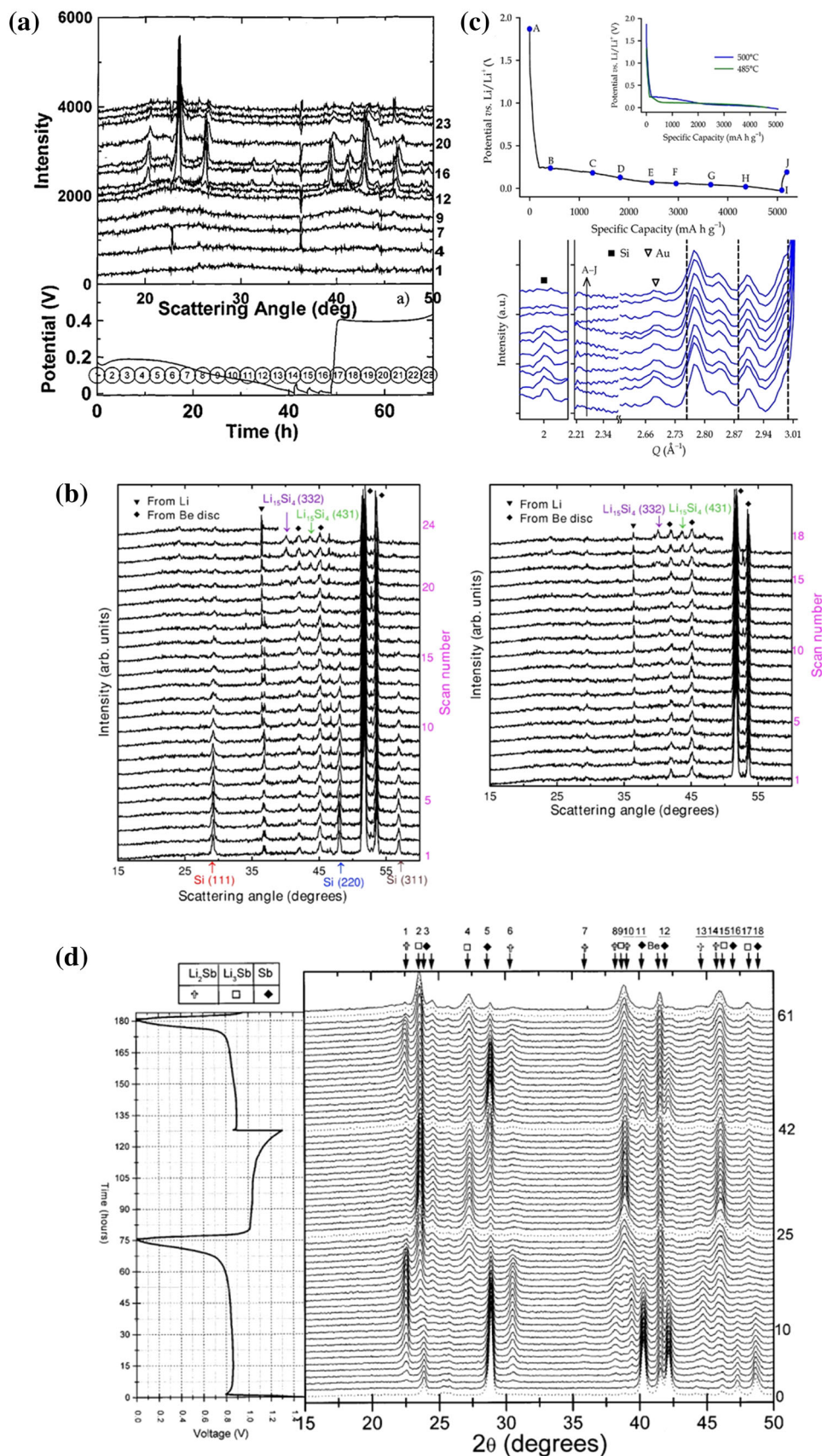ically and economically valuable to meet these demands, or at least theoretically. However, long-time usage of LIB is still a great challenge, due to the capacity fading. The capacity fading is considered resulting from the overcharging, phase transitions, the formation of unstable solid electrolyte interface (SEI), and the dissolution of active materials during electrochemical processes [5]. Apart from that, most electrode materials suffer from poor rate performance. Nevertheless, all these phenomena and possible mechanisms are characterized through the

---

Guobin Zhang and Tengfei Xiong have contributed equally to this work.

Address correspondence to E-mail: xuxu@whut.edu.cn; mlq518@whut.edu.cn

Springer

Figure 1 **a** In situ XRD patterns of amorphous silicon electrode and the discharge/charge profile during the first cycle. **b** In situ XRD patterns of crystalline silicon electrode and the discharge/charge profile during the first cycle. **c** In situ XRD results for a silicon nanowires grown by CVD at 500 °C under electrochemical cycling. **d** In situ XRD patterns of the Sb electrode of a Li/Sb cell. **a** Reproduced with permission from Hatchard and Dahn [21]. **b** Reproduced with permission from Li et al. [23]. **c** Reproduced with permission from Misra et al. [24]. **d** Reproduced with permission from Hewitt et al. [27].

current/voltage curve of battery and some ex situ strategies, which are influenced by the external circumstances greatly. The real-time electrochemical reaction mechanism cannot be obtained unless in situ technology is applied. Thus, researchers have employed in situ detection methods to study these degradation mechanisms. A series of in situ measurements, including in situ X-ray diffraction (XRD), in situ transmission electron microscope (TEM), in situ micro Raman, and in situ X-ray absorption fine structure (XAFS), etc., have been developed and widely applied in the investigation of electrochemical processes. Among these measurements, in situ XRD is considered as one of the best tools to acquire the information of structure evolution for real-time probing. Phase transformations, and crystal evolutions, including lattice constant changes, crystalline state ranges, and intermediate state occurrence of transition, can be directly observed during the electrochemical process, via in situ XRD [6–8]. Meanwhile, phase transformations and volume changes, which can be deducted from the in situ XRD characterization results, are of great significance in achieving excellent cell performance [9–13]. Based on this, considerable research articles in terms of phase evolution process have been published to guide the electrode material design [14]. The recent progresses regarding the employment of in situ XRD method in LIBs and sodium-ion batteries (SIBs) are discussed and summarized in this review. Herein, for LIBs, we divide these progresses into three sections based on the reaction mechanisms: alloying reactions, conversion reactions, and intercalation reactions [15–18]. For SIBs, we divide the researches into cathode materials and anode materials. Finally, the broader use and the future development of in situ XRD are discussed.

In situ XRD in lithium-ion batteries

In the past several decades, considerable papers have been published on the topic of LIB. These researches are aiming to solve some existing problems in LIBs. The performance of the materials is dependent on the structure and reaction processes. So a great number of researches are focused on the mechanism investigation, in which in situ XRD has shown its unique ability in LIB.

Alloying reactions

In the alloying reaction, lithium ions react with the active materials without displacing (extruding) the components from them. The insertion of lithium ions into Si, Sb, and Ge, leads to the alloying reactions. And in situ XRD is very powerful in the investigation of their reaction mechanism.

Si

Among the various kinds of anode materials, silicon has significant advantages, such as low discharge potential and high capacity [19]. As the anode material for LIBs, silicon delivers the potential plateau of about 0.2 V versus Li^+/Li and the theoretical capacity of 4200 mA h g^{-1} [20]. However, its large volume change during the charge/discharge process has hindered its commercialization. In view of this critical issue, some researchers have employed in situ XRD to probe the details including phase evolution in the electrochemical processes. In 2004, Hatchard and Dahn [21] performed in situ XRD to investigate the reaction mechanism of lithium with amorphous silicon. As shown in Fig. 1a, they successfully confirmed the existence of a new crystalline phase $Li_{15}Si_4$ below 30 mV versus Li^+/Li, which was firstly observed by Obrovac and Christensen [22] in the same year. In 2007, Li and Dahn [23] used the crystalline silicon as the anode material and found that amorphous Li_xSi crystallized into $Li_{15}Si_4$ swiftly at about 60 mV versus Li^+/Li (Fig. 1b). In 2012, Misra et al. [24] carried out in situ synchrotron X-ray diffraction on silicon nanowires, and the XRD patterns are demonstrated in Fig. 1c. Their experimental results showed that the $Li_{15}Si_4$ phase can also be avoided by controlling the temperature.

Sb

Sb is an attracting anode material for LIBs due to its high capacity of about 993 mA h g^{-1} [25, 26]. In 2001, Hewitt et al. [27] investigated the reaction mechanism between Li and Sb, which was raised by Wang et al. [28] in 1986. According to the in situ XRD patterns in Fig. 1d, the charge process is not the inverse process of discharge. During the insertion of lithium ions, there are two stages in the discharge curve: firstly Sb converts to Li_2Sb at the voltage of 0.90 V, and then

Li_2Sb converts to Li_3Sb at the voltage of 0.85 V. Unlike the insertion process, the de-insertion process undergoes only one electrochemical stage: the Li_3Sb phase converts to Sb directly without the formation of the intermediate Li_2Sb phase.

Ge

Ge possesses a relatively high theoretical capacity of 8643 mA h cm^{-3} when it transforms to the $Li_{22}Ge_5$ phase [29]. Therefore, it is important to study the reaction mechanism for understanding the electrochemical process of Ge. Ge is often compared with Si, as they are similar in some physical and chemical properties. However, the expansion of Si is anisotropic, while the expansion of Ge is isotropic upon lithiation/de-lithiation [30, 31]. Therefore, the detail electrochemical reaction mechanism of Ge with Li would be different from that of Si. In 2009, Baggetto and Notten [32] utilized in situ XRD to detect the reaction mechanism between Ge thin film and Li in detail. They tried to investigate two kinds of films: evaporated film and sputtered film, respectively. The results in Fig. 2 show that both of the two Ge films formed the amorphous phase Li_xGe firstly and then crystallized into the cubic $Li_{15}Ge_4$ (with the maximum capacity of 1385 mA h g^{-1}) with full insertion of lithium ions. Also, they found that the electrochemical performance of evaporated Ge thin film is better than the sputtered one.

Conversion reactions

Electrode materials undergo a conversion reaction with Li often store more than one Li atom per molecular, and are the one of the most interesting candidates for high-capacity cathodes for LIBs. Conversion reactions often happen when lithium ions insert into the metal oxides and metal sulfides, including Fe_3O_4, RuO_2, $Co_2V_2O_7$, and CuS, etc.
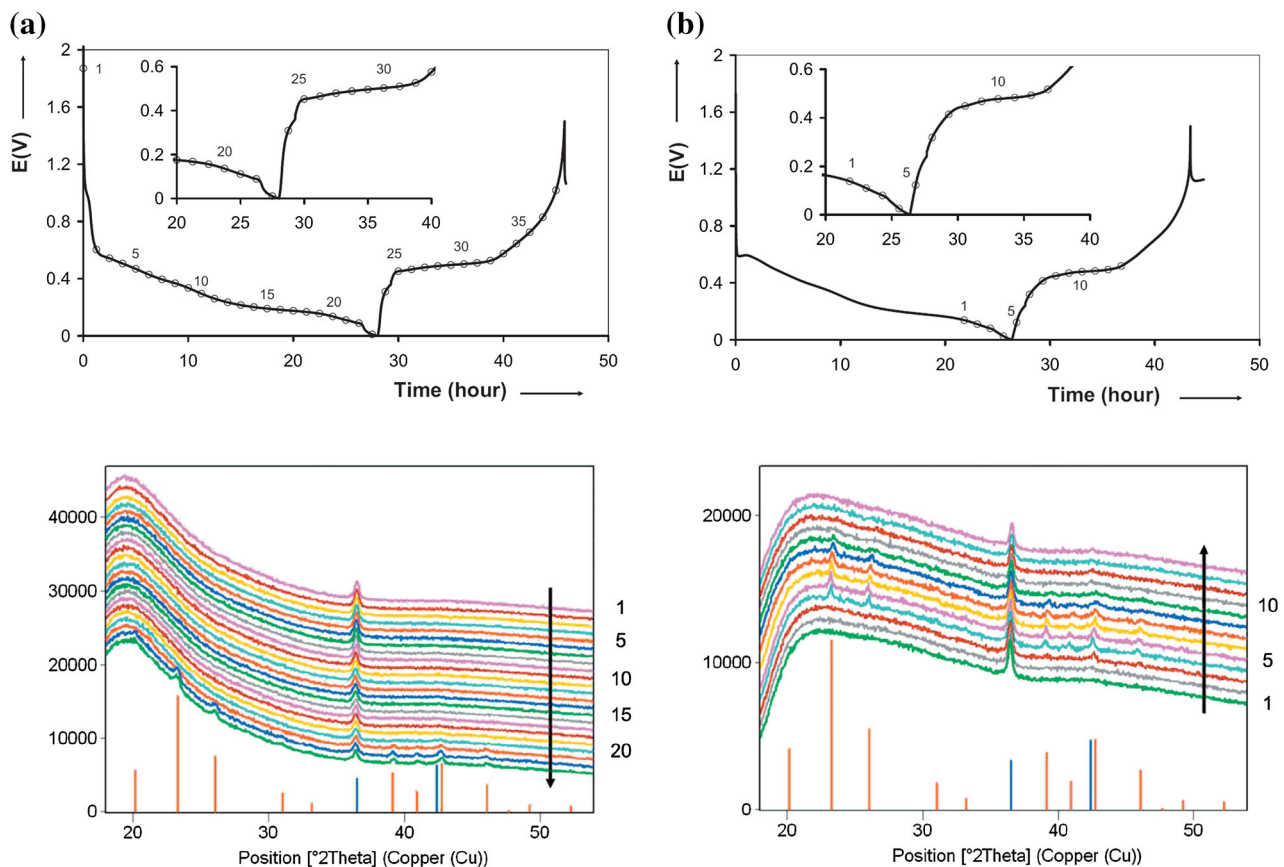

Figure 2 **a** In situ XRD characterization of a 200 nm thick evaporated Ge film. **b** In situ XRD characterization of a 200 nm thick sputtered Ge film. Reproduced with permission from Baggetto and Notten [32].

Fe₃O₄

Conversion reactions usually lead to high capacity in anode materials, such as Fe_3O_4. Apart from the high theoretical capacity of 928 mA h g^{-1}, Fe_3O_4 is also highlighted for its elemental abundance, low cost as well as low toxicity [33–35]. However, this promising material has its drawbacks in several aspects, especially the large volume change and the low coulombic efficiency in the first cycle. To solve these problems, various methods have been used to enhance the structural stability and detect the reaction mechanism of Fe_3O_4-based electrode materials [36]. An et al. [37] designed a facile process to synthesize the hierarchical porous Fe_3O_4/graphene nanowires, which are supported by the amorphous vanadium oxide matrixes. The designed porous structure exhibited a high coulombic efficiency, excellent cycling performance, and outstanding reversible specific capacity (1146 mA h g^{-1}). In order to explore the phase evolution involved in this porous Fe_3O_4-based material, in situ XRD measurement was implemented (as shown in Fig. 3a). In the initial discharge process, the two peaks at 30.1 and 35.5° [corresponding to (220) and (311) planes of Fe_3O_4, respectively] both shifted to a lower angle continuously with the lithium-ion insertion. In the meantime, these two peaks became weaker and weaker, and then totally disappeared in the following stages. Therefore, the conclusion can be made that the insertion of lithium ions brings about the volume expansion as well as the amorphous transformation of Fe_3O_4.

RuO₂

In recent years, the RuO_2 anode material arouses huge interests among researchers for its metal-like electrical conductivity, high capacity, and unique lithium-storage mechanism, which involves the "additional capacity." [38–40]. The "additional capacity" means that the experimental capacity beyond the stoichiometric conversion limits of RuO_2. According to the conversion reaction, the theoretical capacity of RuO_2 is 806 mA h g^{-1}. However, the highest capacity ever reported for this material is 1310 mA h g^{-1}, which could be explained by a more complicated mechanism [40]. In order to probe the origin of the additional capacity, Kim et al. [41] employed in situ XRD to investigate the reaction mechanism between Li and RuO_2 under deep discharge. The result is revealed in Fig. 3b. At the start of the discharge process, RuO_2 transforms to $LiRuO_2$ accompanied by the intermediate phase Li_xRuO_2. Further insertion of lithium ions facilitates the conversion reaction, during which $LiRuO_2$ decomposes to nanosized Ru and Li_2O. The additional capacity shown in the last discharge process with the voltage below 0.5 V, is not given by the conversion reaction. A combination of X-ray absorption spectroscopy, the electrochemical techniques, and the in situ XRD verified that it is the grain boundary between Ru and Li_2O contributes to the high capacity. Furthermore, the work by Hassan et al. [42] proved that this phenomenon is not unique. By studying the lithium sorption in RuO_2, SnO_2, and SnS_2, they found that the mechanism of interfacial
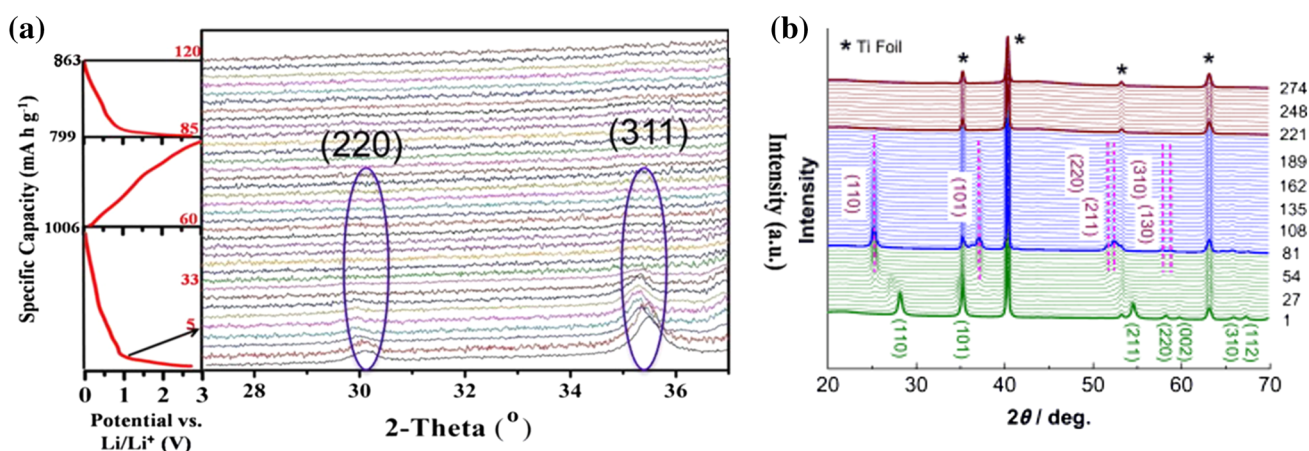

Figure 3 **a** In situ XRD patterns of amorphous vanadium oxides matrixes supporting hierarchical porous Fe3O4/graphene nanowires. **b** In situ XRD patterns collected during the discharge of a RuO₂ anode. **a** Reproduced with permission from An et al. [37]. **b** Reproduced with permission from Kim et al. [41].
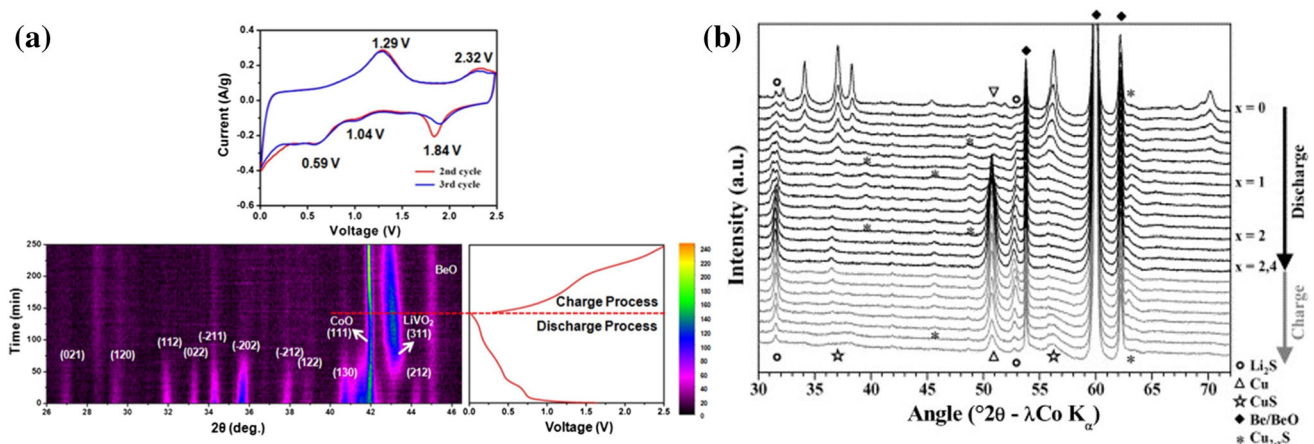
(a)

(b)

Figure 4 a In situ XRD patterns of hierarchical $Co_2V_2O_7$ nanosheets and the second and third cycles of cyclic voltammetry curves at a sweep rate of 0.1 mV/s in the potential range from 0.01 to 2.5 V versus Li^+/Li. **b** In situ X-ray diffraction performed on Li/CuS electrochemical cell cycled at C/5 in the first cycle. **a** Reproduced with permission from Luo et al. [45]. **b** Reproduced with permission from Débart et al. [52].

storage is common for materials including metal oxides and metal sulfides.

$Co_2V_2O_7$

As an important cobalt vanadate, one $Co_2V_2O_7$ molecule can accommodate 13.6 lithium ions during the first discharge process in the voltage range of 0.02–3.5 V [43]. Recently, its performance has been improved greatly by Wu et al. [44] They successfully synthesized the mesoporous $Co_2V_2O_7$ monodisperse hexagonal nanoplates, which maintained a reversible capacity of 866 mA h g^{-1} at a current density of 500 mA g^{-1}. The high capacity has made $Co_2V_2O_7$ a potential anode material for lithium-ion batteries. Afterward, Luo et al. [45] obtained a novel hierarchical $Co_2V_2O_7$ nanosheet with excellent electrochemical performance by a facile synthesis method. In order to determine the reaction details, in situ XRD method was used, as shown in Fig. 4a. Combined with the charge–discharge curve in the first cycle, it is concluded that the second plateau at 0.4 V corresponds to the decomposition of $Co_2V_2O_7$ and the lithiation of V_2O_5 (to form $LiVO_2$). Further insertion of lithium ions at about 0.16 V results in the reduction from CoO to Co and the lithiation of $LiVO_2$ to form $Li_{1+x}VO_2$ [46, 47]. The electrochemical reactions of $Co_2V_2O_7$ are analogous to that of the $Co_3V_2O_8$ [48].

CuS

Metal sulfides are promising anode materials for lithium batteries for their high specific capacity, good rate capability, and low cost [49, 50]. Among them, copper sulfide is highlighted for its good electrical conductivity and flat discharge curves [51]. The reaction mechanism between copper sulfide and lithium ions, is proved to be complex and hard to observe. In 2006, Débart et al. [52] studied the electrochemical reactivity of transition metal (cobalt, nickel, and copper) sulfides. In this study, they found that lithium ions react with cobalt sulfide or nickel sulfide through a conversion reaction. However, using in situ XRD, different mechanisms are detected in copper sulfide. From Fig. 4b, CuS reacts with lithium ions through a displacement reaction, which is accompanied by the formation and disappearance of large Cu dendrites. The whole process proceeded via the intermediary phase $Cu_{1-x}S$. Based on the determined mechanism, various subsequent researches focused on the performance improvement of copper sulfides by solving the problems such as large volume change. The wrapping strategies with the guidance of this in situ probing analysis are widely employed, and the results show that the utilization of graphene [53, 54] and copper can enhance the cycling performance obviously.

Intercalation reactions

Intercalation reactions happen in most cathode materials and some anode materials with stable structures, including TiO_2, Li_3VO_4, MnO_2, MoO_3, $LiMn_2O_4$, and $LiFePO_4$.

Negative electrode materials

Anatase TiO_2 Despite the relatively low theoretical capacity, anatase TiO_2 has become one of the most promising anode materials for LIBs. Its structural stability, abundant resources, low cost, nontoxicity, chemical safety, suitable working voltage as well as good cycling performance make it an attracting subject to researchers [55, 56]. In 2007, Wagemaker et al. [57] found the impact of particle size on lithium-ion insertion with the example of anatase Li_xTiO_2. Their work has shown that the first-order phase transition witnesses no concomitant phases in particles with size <40 nm. In 2014, Shen et al. [58] employed in situ XRD to further investigate the size-dependent non-equilibrium phase transition of anatase upon

lithiation. The process is shown in Fig. 5a. Even at the very low discharge rate of C/120, the phase transition in anatase TiO_2 is found to be a nonequilibrium process. The experimental result demonstrated that the nanosized anatase exhibits better performance than the microsized anatase. According to the size-dependent behavior, this result originates from the sluggish lithium-ion diffusion in microsized anatase TiO_2. This work offers a perspective that improving interstitial diffusion is quite effective to enhance the rate performance of anatase TiO_2.

Li_3VO_4 Li_3VO_4 attracts much attention as the anode material for lithium batteries in recent years [59]. One obvious advantage of this material is its high ion conductivity. Besides, it is also attractive for the high theoretical capacity and suitable voltage plateau. The main drawback of Li_3VO_4 is its poor electrical conductivity, which leads to poor cycling performance [59]. In the past few years, much work has been done to improve the electrochemical performance or to probe the reaction mechanism of Li_3VO_4. In 2015, Liang et al. [60] synthesized the carbon-coated
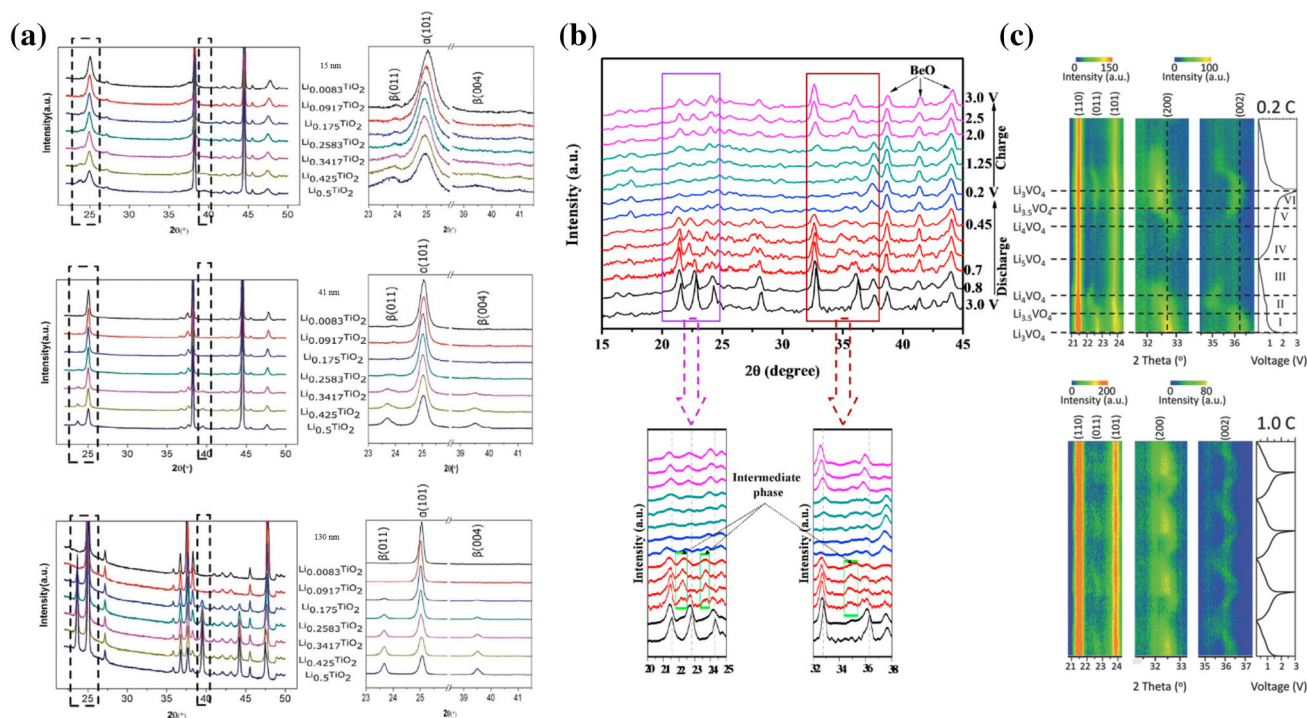

Figure 5 **a** In situ XRD patterns of Li_xTiO_2 obtained at different states of first discharge for three particle sizes. **b** In situ XRD patterns of electrochemically cycled Li_3VO_4/C anode during the first cycle. **c** In situ XRD patterns collected during galvanostatic discharge/charge of the Li_3VO_4/C/rGO half-cell at 80 mA g^{-1} (0.2

C) and 400 mA g^{-1} (1.0 C) respectively. **a** Reproduced with permission from Shen et al. [58]. **b** Reproduced with permission from Liang et al. [60]. **c** Reproduced with permission from Li et al. [61].

Li_3VO_4 by a solid-state method. By the in situ XRD characterization in Fig. 5b, they firstly offered the direct observation that Li_3VO_4/C reacts with Li via a reversible insertion/de-insertion process. In their research, the whole discharge process is divided into three parts: the initial solid-solution stage, the second two-phase stage accompanied by an intermediate phase, and the last stage when the final new phase is formed. Upon charge, the intermediate phase formed in the second stage does not appear. Li et al. [61] also utilized in situ XRD to analyze the mechanism involved in the mesoporous $L_3VO_4/C/rGO$ nanocomposite (Fig. 5c). The obtained two-dimensional XRD patterns are in accordance with Liang's work. In addition, Li acquired the in situ XRD patterns at a relatively high current density, which shows a continuous shift during whole discharge process. It is confirmed that this nonequilibrium solid-solution process is also highly reversible. Recently, Zhou et al. [62] combined in situ XRD with in situ EIS to study the structure changes as well as the interfacial properties of Li_3VO_4. They discovered that the irreversible phase transformation occurs during the initial charge/discharge process, which is another reason for the low initial coulombic efficiency besides the SEI formation.

Positive electrode materials

The cathode material is a key component and the development bottleneck of the LIBs. Exploring the reaction mechanism can contribute to the development of LIBs with high performance.

MnO_2 MnO_2 is a functional metal oxide widely applied in fields such as ion exchange, molecular adsorption, catalysis, and biosensor [63]. Apart from these, MnO_2 is also an excellent electrode material in lithium batteries for its low cost, high safety, natural abundance, and especially high theoretical capacity [64, 65]. During lithiation or de-lithiation, the valence of Mn changes between +3 and +4. However, the poor kinetics, the irreversible transformation, large volume change, and the complex reaction mechanism have restricted its further development [66]. In some researches, alkaline or alkaline-earth elements are used to stabilize this material, pursuing enhanced electrochemical performance [65, 67]. Pang et al. [68] used in situ synchrotron XRD to observe the reaction mechanism upon the lithiation of cryptomelane $K_{0.25}Mn_2O_4$, which is a manganese oxide similar to α-MnO_2 with I4/m tetragonal structure. As shown in Fig. 6a, the intercalation and de-intercalation of lithium ion in this structure follows a solid-solution path, with the variation of parameters *a* and *c*. In addition, the reversible strain effect caused by Jahn–Teller distortion is also determined.

MoO_3 MoO_3 is a promising material with the applications in lubricants, sensors, optical devices, photochromic devices, catalysts as well as energy-storage devices [69, 70]. Among various transition-metal oxides, nanosized MoO_3 has been extensively studied for its multi-electron reaction character of Mo in the electrochemical process. There are two types of MoO_3: the α-type and the β-type [71]. The α-type of MoO_3 is a layered orthorhombic phase, which can
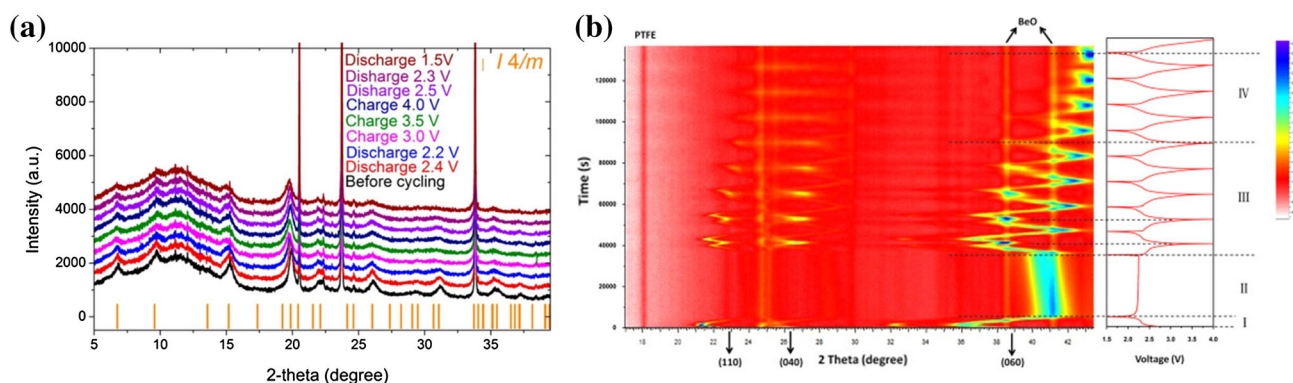

Figure 6 **a** Stack of selected synchrotron X-ray diffraction patterns of the customized cell containing $K_xMn_2O_4$ cathode and Li anode collected at various states of charge. **b** In situ XRD patterns of Na–Mo–O electrode and the corresponding charge/ discharge profile during the initial nine cycles. **a** Reproduced with permission from Pang et al. [68]. **b** Reproduced with permission from Dong et al. [75].

store lithium ions at interlayer and intralayer sites. And as a general case, the lithiation into the interlayer sites only occurs during the initial discharge, which results in an irreversible structure rearrangement [72]. Besides, the low conductivity also accounts for the fast capacity fading of MoO_3. Therefore, some researchers are aiming at improving its conductivity [73], and others utilize the inhibiting effect of proper metal ions to stabilize the host structure [74]. Dong et al. [75] synthesized a Na^+ pre-intercalated MoO_3 nanobelt via a facile method and used in situ XRD to investigate the inhibiting effect of Na^+ in the interlayers. Figure 6b shows, in the first discharge process, the lithiation leads to an interesting expansion/contraction process of the layered structure. The contraction would originate from the distortion of the Mo–O bonds upon the strong attraction of lithium ions. Then, with the de-intercalation driven by charge, the interlayer spacing expands as expected. Although some sodium ions extracted from the host structure together with the de-intercalation of lithium ions, their inhibiting effect is still obvious to some extent. This work testified that the "preintercalation" is an effective method to stabilize the layered structure of MoO_3.

Vanadium oxides Vanadium oxides, such as V_2O_5, VO_2, V_2O_4, V_2O_3, and V_6O_{13}, are a series of electrode materials for lithium batteries, featuring high energy density, moderate voltage plateau, abundant resources, low cost, high safety, and facile preparation methods [76–78]. However, in view of the poor rate performance and structural stability of vanadium oxides, alkali ions have been used as "pillars" to

stabilize the host structures [79, 80]. That is to say, vanadates should have better electrochemical performance. Based on this idea, many researchers focus their attention on various vanadates: design new structures and probe the reaction mechanism. Meng et al. [81] synthesized three vanadium-based nanowires (V_2O_5, KV_3O_8, and $K_{0.25}V_2O_5$), with $K_{0.25}V_2O_5$ exhibiting the best performance. With the help of the in situ XRD patterns in Fig. 7, they proved that the excellent performance of $K_{0.25}V_2O_5$ originates from the "inhibiting effect" of K ions in the layered structure. Niu et al. [82] designed a three-dimensional V_2O_5/NaV_6O_{15} hierarchical heterostructure through controlling the nucleation and growth process. The distinct plateaus and the slight shift of the in situ XRD patterns proved the fast and stable kinetic process of this 3D structure. Yan et al. [83] studied the structural change of $Na_{0.76}V_6O_{15}$ nanorods in two different voltage windows under *operando* conditions. Structure refinement verified the existence of ionized oxygen when charged to 2.0 V. Moreover, deep charge to 1.5 V leads to amorphization and irreversible reaction pathway, which further results in low electrical conductivity and fast capacity fading.

LiMn₂O₄ The remarkable advantage of $LiMn_2O_4$ is its high cell voltage, which makes it one of the most promising cathode materials for batteries in electric vehicles [88]. However, the bad performance at elevated temperature, the decomposition of the electrolyte at high voltage, the Jahn–Teller distortion in deep discharge, and dissolution of the active material remain to be solved [84, 85]. In 2006, Chung et al. [86] adopted in situ synchrotron XRD to study the
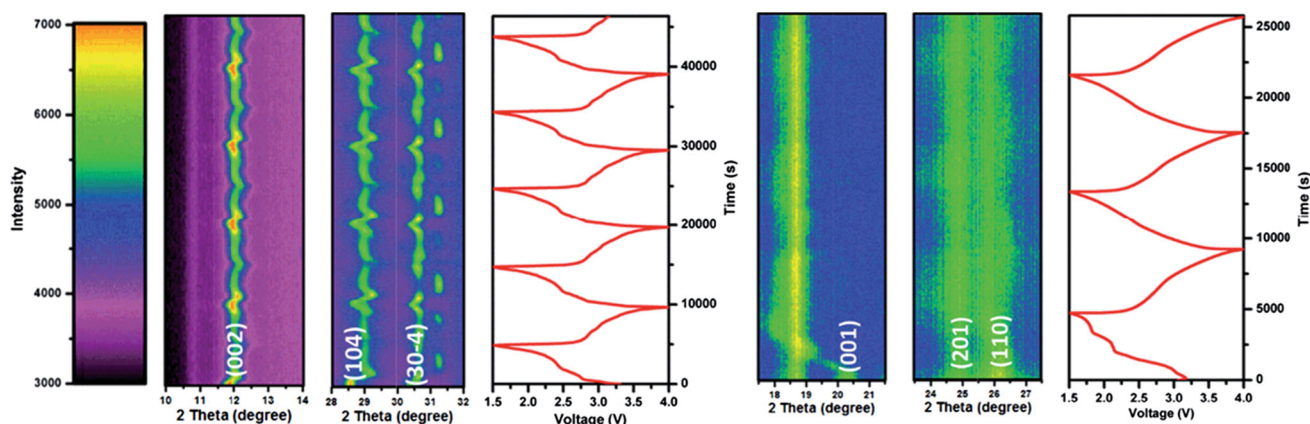

Figure 7 In situ XRD patterns of $K_{0.25}V_2O_5$ nanowires (*left*) and V_2O_5 nanowires (*right*) during galvanostatic charge and discharge at 150 mA g^{-1} in lithium-ion batteries. Reproduced with permission from Meng et al. [81].
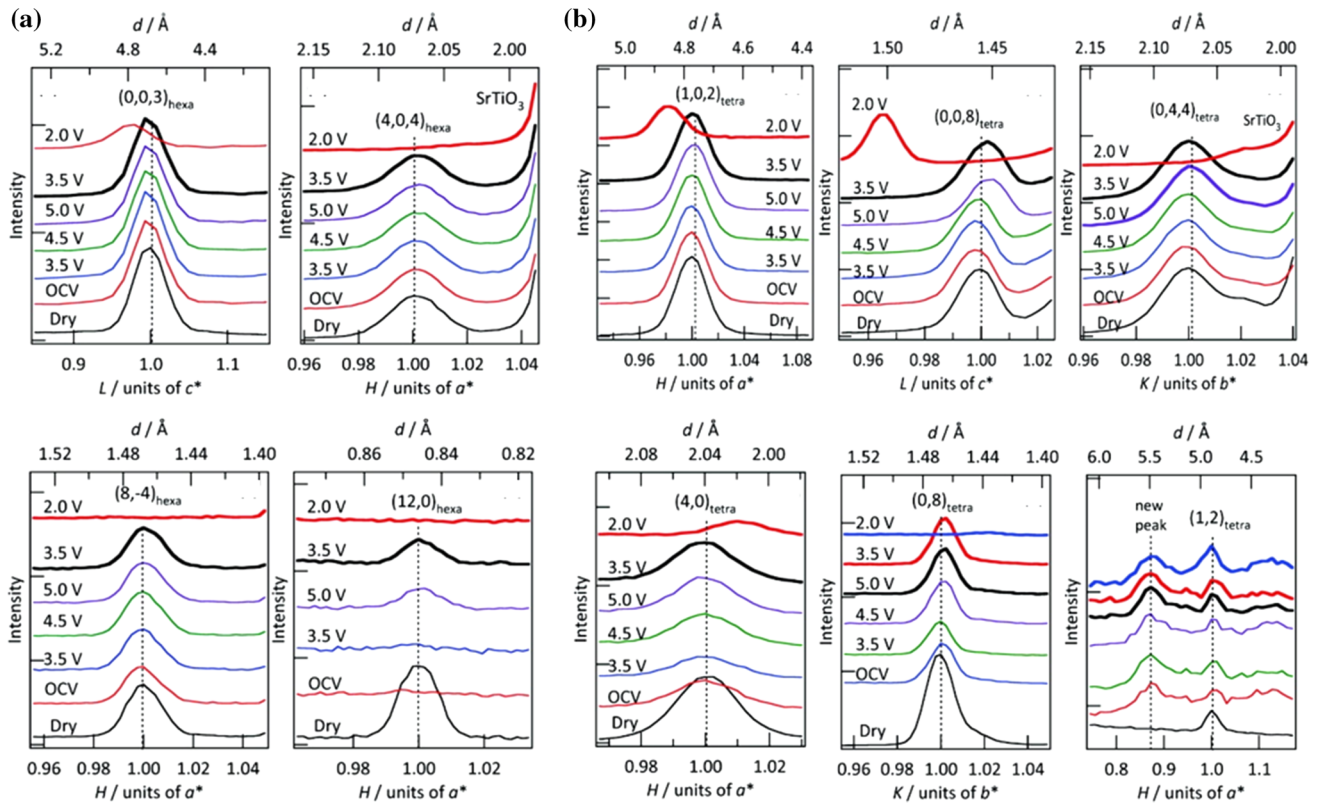
Figure 8 **a** In situ XRD patterns for $LiMn_2O_4$ (111) during the first charge–discharge cycle. **b** In situ XRD patterns of $LiMn_2O_4$ (110) during the first charge–discharge cycle. Reproduced with permission from Hirayama et al. [87].

structure evolution of $LiMn_2O_4$ at elevated temperature, which is accompanied by an obvious capacity fading process. They found that both overcharging to 5.2 V and applying a high temperature of 55 °C contribute to the residue structures. Fortunately, the addition of a tris (pentafluorophenyl) borane (TPFPB) compound in the electrolyte reduces the residues. In 2010, Hirayama et al. [87] employed in situ synchrotron XRD to reveal the structural changes at the interface between $LiMn_2O_4$ and the electrolyte. The mechanism is illustrated in Fig. 8. According to the results, the surface structure begins to change with the creation of an electric double layer and reconstructs once the voltage is applied. Thus, the rate of SEI formation and the stability of the reconstructed surface have influences on the electrochemical performance of $LiMn_2O_4$.

LiFePO₄ Owing to its high power, low cost, excellent thermal stability, $LiFePO_4$ has become a very

fascinating cathode material for electric and hybrid-electric vehicle batteries since the pioneering work of Goodenough [88]. In fact, years' research has improved this material's performance to nearly the peak and its left problems lie in the reaction mechanism. Many researchers try to investigate the mechanism thoroughly via various advanced characterization methods, among which the in situ XRD is quite effective [89, 90]. In 2008, by in situ XRD, Gibot et al. [91] demonstrated the single-phase process of nanosized $LiFePO_4$ upon lithium-ions insertion/extraction at room temperature, which is shown in Fig. 9a. Anyhow, the result is astounding because its generally believed that $LiFePO_4$ stores lithium through a two-phase transition between $LiFePO_4$ and $FePO_4$ [92]. This work indicated that tuning the size can lead to a different phase transition mechanism. In 2011, Malik et al. [93] verified that the outstanding rate capability of $LiFePO_4$ originates from the existence of a single-phase transformation pathway, with only small overpotential required at room
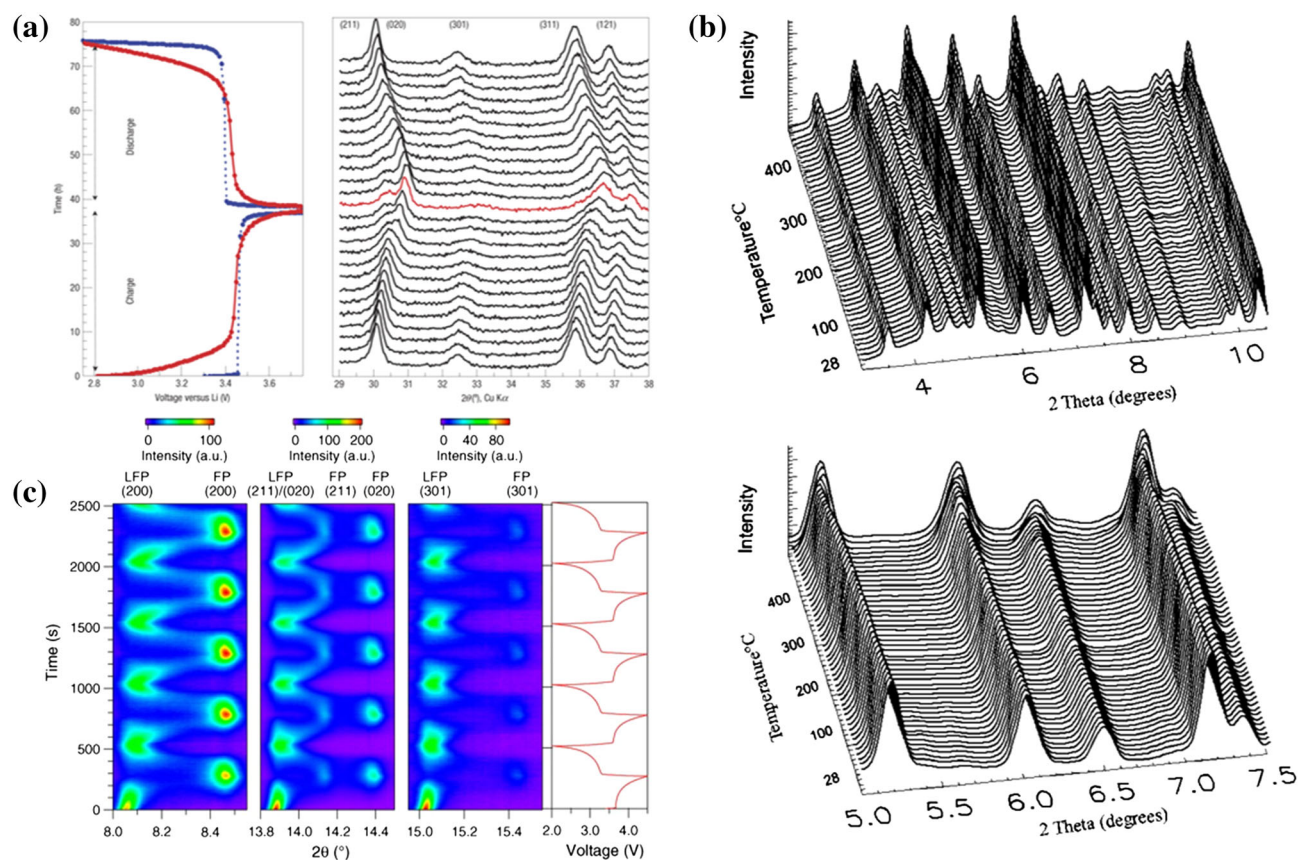
Figure 9 a In situ XRD measurements of 40 nm LiFePO₄ and charge/discharge galvanostatic curves of 40 nm LiFePO₄ (*red line*) and 140 nm LiFePO₄ (*blue line*) at C/40. **b** In situ high-resolution synchrotron XRD patterns from hydrothermally synthesized LiFePO₄ during heat treatment and expanded region of the XRD pattern (2θ: 5–7.5°). **c** In situ XRD patterns of LiFePO₄ during galvanostatic charge and discharge at a rate of 10 C. **a** Reproduced with permission from Gibot et al. [91]. **b** Reproduced with permission from Chen et al. [94]. **c** Reproduced with permission from Liu et al. [95].

temperature. Consequently, to search for high-power energy- storage material, attention should be paid to those with non-equilibrium reaction paths under a minimal overpotential. In the same year, Chen and Graetz [94] utilized the high-resolution synchrotron X-ray diffraction, and the XRD patterns in Fig. 9b reveal the elimination of antisite defects when temperature is raised above 500 °C. In 2014, Liu et al. [95] certified that apart from reducing the particle size, high-rate cycling can also bring about the existence of nonequilibrium solid-solution process in LiFePO₄ (shown in Fig. 9c). In 2016, in consideration of the unsatisfactory low-temperature performance of LiFePO₄, Yan et al. [96] employed in situ XRD to observe the temperature-dependent phase evolution in Li$_x$FePO₄. On the basis of the results, it is concluded that the existence of intermediate greatly enhances the diffusion kinetics of Li$_x$FePO₄ at low temperature.

In situ XRD characterization of sodium-ion batteries

In view of the limited lithium resource on earth, SIBs have attracted increasing attention in the past few years. With a larger radius, sodium ion migrates more slowly than lithium ion and causes larger structure change during insertion/de-insertion, which further limits the rate capability and cycling performance greatly. In addition, this difference in radius may lead to new reaction mechanism.

Negative electrode materials

Sn

Chevrier and Ceder [97] predicted that Sn can react with Na to deliver a theoretical capacity of 851 mA h g^{-1}, with the formation of Na₁₅Sn₄. The

improvement in cycling performance with the precondition of high capacity has made Sn one of the most prominent anode materials for SIBs [98, 99]. In 2012, Ellis et al. [100] utilized in situ XRD to observe the reversible insertion of sodium in Sn. The corresponding voltage curves show four distinct plateaus, indicating four two-phase processes upon sodiation. As gathered in Fig. 10a, the XRD patterns demonstrated that full sodiation leads to the ultimate phase $Na_{15}Sn_4$, in good accordance with the discharge capacity of 847 mA h g^{-1}. The left three phases are new that have not predicted by the phase diagram, among which one is amorphous, near the composition NaSn. Low atom mobility of this composition may account for the amorphism.

$Na_2Ti_3O_7$

Considering the lithium insertion compound with very low potential versus Na^+/Na, $Na_2Ti_3O_7$ is a promising candidate. This compound has long been investigated in the fields of sensors, catalysis, waste removal, and LIBs for its structural feature [101]: zigzag layers of titanium oxygen octahedra together with the sodium ions in the interlayer constitute the structure [102]. In 2011, Senguttuvan et al. [103] first reported the electrochemical tests of this material as the anode for sodium batteries, and in situ XRD measurement was also implemented. At the plateau 0.3 V versus Na^+/Na, according to the three peaks at 33.9, 39.2, and 40.7° in Fig. 10b, a new phase emerges and strengthens while the primitive phase disappears gradually. When the oxidation process ends, no $Na_4Ti_3O_7$ phase is identified, which suggests the good reversibility process of the sodium insertion/de-insertion. Since this initial research, different structures of $Na_2Ti_3O_7$ have been designed to enhance its electrochemical performance in sodium batteries [104, 105].

$NaTi_2(PO_4)_3$

In recent years, the NASICON (Na-Superionic Conductor) structural compounds with polyanions have been intensively studied for their potential applications in SIBs and supercapacitors [106, 107]. These compounds feature the large interstitial channels to constitute the 3D open structure, such as $NaTi_2(PO_4)_3$. Besides, $NaTi_2(PO_4)_3$ is also stable, cheap, and environmentally friendly. However, the poor electrical conductivity, which leads to poor rate capability, is a crucial problem facing this material. So many researchers focus on improving the electrical conductivity of $NaTi_2(PO_4)_3$ [108, 109]. Xu et al. [110] designed a carbon-coated hierarchical $NaTi_2(PO_4)_3$ mesoporous microflowers with excellent rate performance. *Via* the in situ XRD measurement in Fig. 11, the electrochemical reaction is determined to be a two-phase reaction in the voltage range from 1.5 to 3.0 V. All of the characteristic peaks of $NaTi_2(PO_4)_3$ become weaker with the Li insertion, accompanied by the expansion of the lattice spacing, such as (113), (024), and (116). In the meantime, new peaks emerge gradually, indicating the formation of $Na_3Ti_2(PO_4)_3$. The process is highly reversible because no $Na_3Ti_2(PO_4)_3$ phase remains at the end of the charge process.

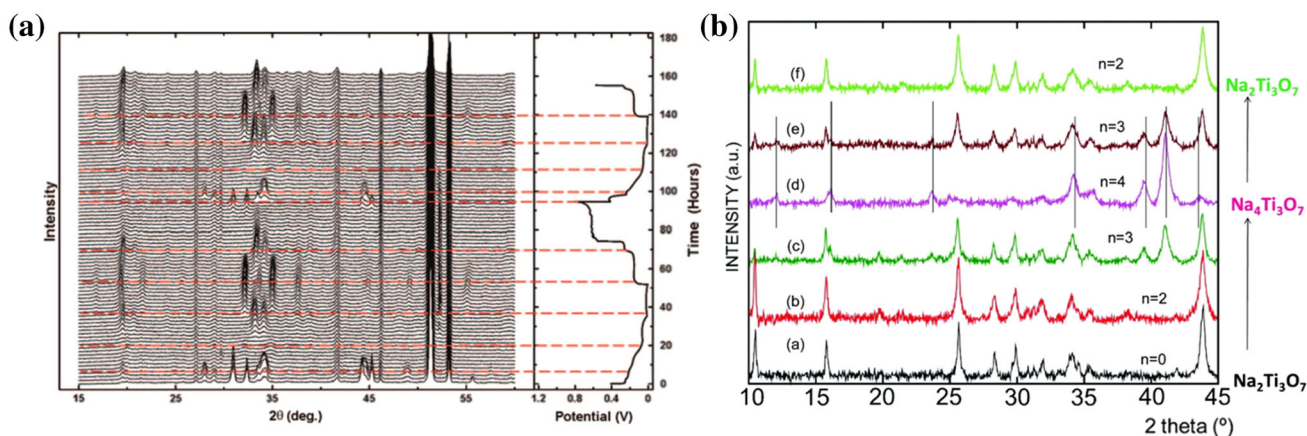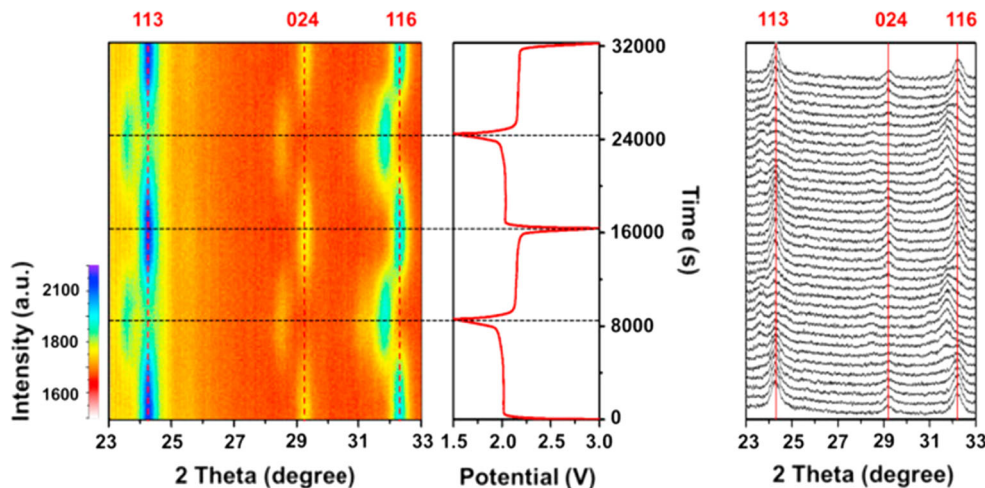**Figure 10 a** In situ XRD data and the corresponding voltage curve of Sn electrode. **b** In situ XRD study of a $Na_2Ti_3O_7/Na$ cell cycled between 2.5 and 0.01 V at a C/50 rate. **a** Reproduced with permission from Ellis et al. [100]. **b** Reproduced with permission from Senguttuvan et al. [103].

Figure 11 In situ XRD patterns of the NTP/C-F(carbon-coated hierarchical $NaTi_2(PO_4)_3$ mesoporous microflowers) half cell during galvanostatic discharge and charge at 50 mA g^{-1} and a voltage range of 1.5–3.0 V. Reproduced with permission from Xu et al. [110].

2D transition metal dichalcogenides

Two-dimensional transition metal dichalcogenides MX_2 (M = Mo, W, Ti, V, Nb, etc.; X = S, Se, Te) are formed by layers of X-M-X atomic slabs, which are linked by the weak van der Waals force [111]. The large slab spacing allows Na$^+$ to intercalate/de-intercalate fast and reversibly. Besides, the ion X^{2-} can stabilize the intercalation or de-intercalation process of Na ions [112]. Among these compounds, MoS_2 shows great potential in SIBs. According to the results from Wang et al. [113], the in situ XRD data indicates that two-phase transitions occur upon sodiation under 1 V versus Na$^+$/Na (illustrated in Fig. 12a). The first transition is from 2H-MoS_2 to 2H-$Na_{0.5}MoS_2$ and the second to 1T-$NaMoS_2$. Insertion of more Na$^+$ after the second plateau leads to no obvious structural change. The subsequent discharge process starts with a solid-solution reaction. Till charging to 2.5 V, a two-phase transition appears from 1T-$Na_{0.5}MoS_2$ to 1T-MoS_2. The work done by Ou et al. [114] in Fig. 12b tracked the electrochemical process of chemically exfoliated NbS_2. XRD patterns verify that the NbS_2 sheets undergo a reversible solid-solution reaction, a feature which is beneficial for high electrode performance. This result is also in good accordance with the calculation predictions performed by Jung et al. [115].

Positive electrode materials

The limit of SIBs' development is set by its cathode materials. Exploring the reaction mechanism of cathode materials with in situ observation helps to develop better SIBs.
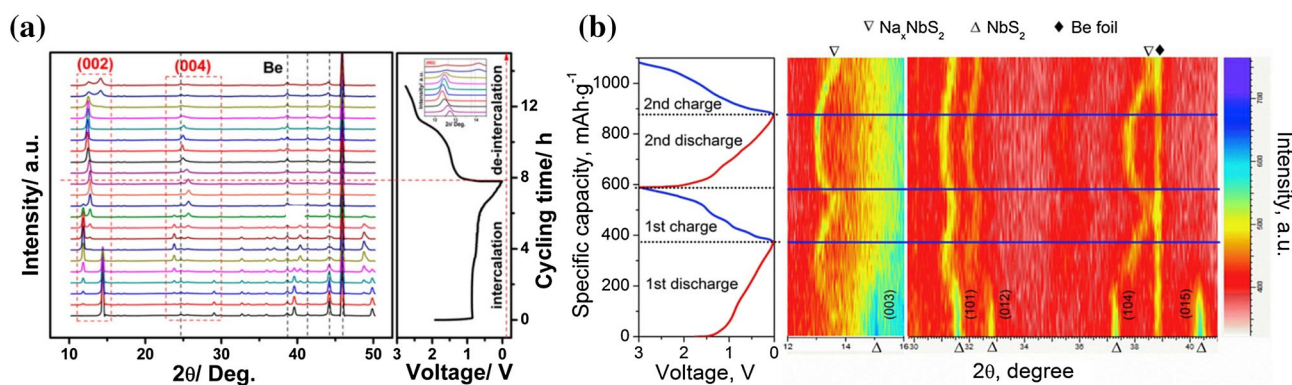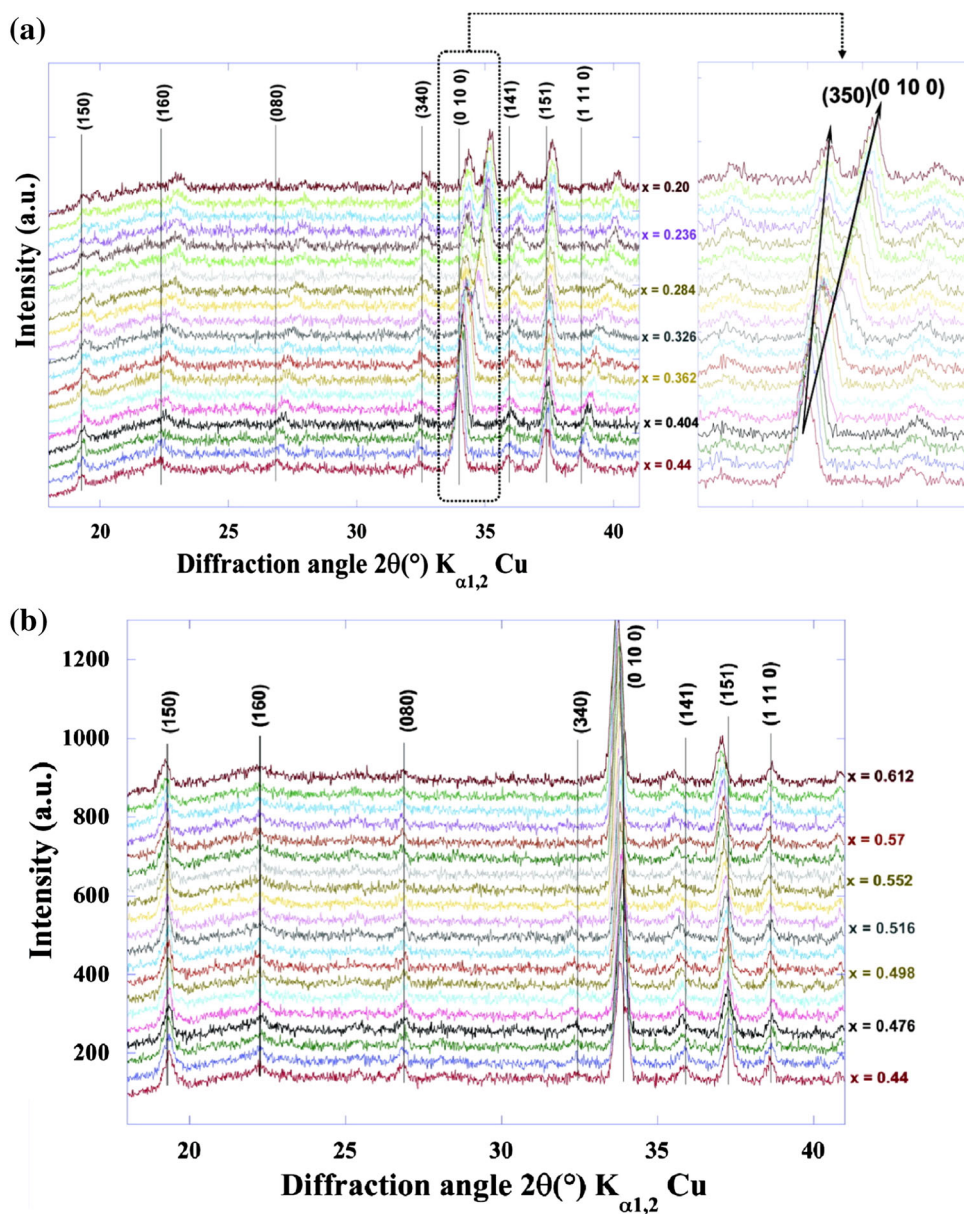

Figure 12 **a** In situ XRD patterns of commercial MoS_2 containing different contents of electrochemically intercalated Na ions. **b** First two-cycle charge–discharge curves and the corresponding in situ XRD patterns collected between 0.01 and 3.0 V at 0.1 A g^{-1} of chemically exfoliated NbS_2 nanosheets based anode. **a** Reproduced with permission from Wang et al. [113]. **b** Reproduced with permission from Ou et al. [114].

Figure 13 In situ evolution of the XRD patterns recorded at a C/250 charge/discharge rate: **a** upon reduction and **b** upon oxidation of $Na_{0.44}MnO_2$. Reproduced with permission from Sauvage et al. [119].

$Na_{0.44}MnO_2$

Among various cathode materials for SIBs, $Na_{0.44}MnO_2$ has its distinct advantages in several aspects: a high specific capacity of 120–130 mA h g^{-1} [116], and good cycling performance after being nanosized as well as the potential to be applied in aqueous electrolyte [117]. Despite these advantages, the applications of $Na_{0.44}MnO_2$ are still largely hindered by the complex reaction which needed to be solved by the related reaction mechanism [118]. Sauvage et al. [119] combined in situ XRD with potentiostatic intermittent titration to detect the phase transition process of

$Na_{0.44}MnO_2$ with the potential ranging from 2 to 3.8 V (vs. Na^+/Na). The results in Fig. 13 indicate that six biphasic reactions appear in the whole process. For the Na_xMnO_2 system, the insertion of sodium ion is fully reversible in the range of $0.25 < x < 0.65$.

Vanadate phosphates

$Na_3V_2(PO_4)_3$ is an outstanding energy storage material for SIBs, which features excellent structural stability and high ion conductivity due to its unique three-dimensional open frameworks (known as
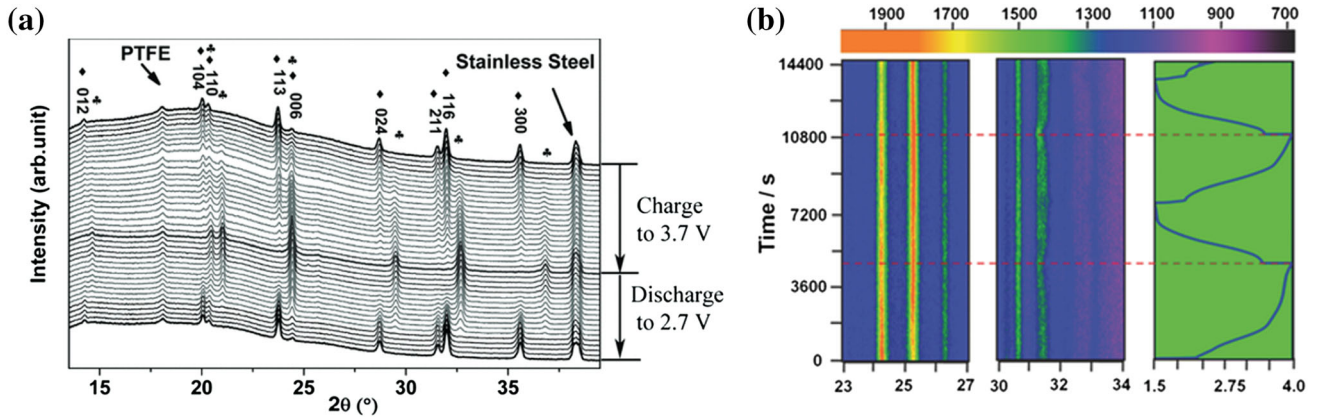
Figure 14 a In situ XRD patterns of the $Na_3V_2(PO_4)_3$/Na cell cycled between 3.7 and 2.7 V at a current rate of C/10. *Black diamond suit* represents $Na_3V_2(PO_4)_3$ and *black club suit* represents $NaV_2(PO_4)_3$. **b** In situ XRD patterns of $K_3V_2(PO_4)_3$/C bundled nanowire during galvanostatic charge and discharge at 100 mA g^{-1}. **a** Reproduced with permission from Jian et al. [122]. **b** Reproduced with permission from Wang et al. [123].

NASICON structure) [120]. Furthermore, this material exhibits a high theoretical specific capacity up to 118 mA h g^{-1} [121] and a relatively high voltage plateau of 3.4 V. In 2013, Jian et al. [122] firstly employed in situ XRD technique to determine the reaction mechanism of sodium insertion/extraction of this compound at a low current rate (shown in Fig. 14a). When charged to 14 mA h g^{-1}, several new peaks occur and strengthen while original peaks weaken gradually, which is a typical two-phase
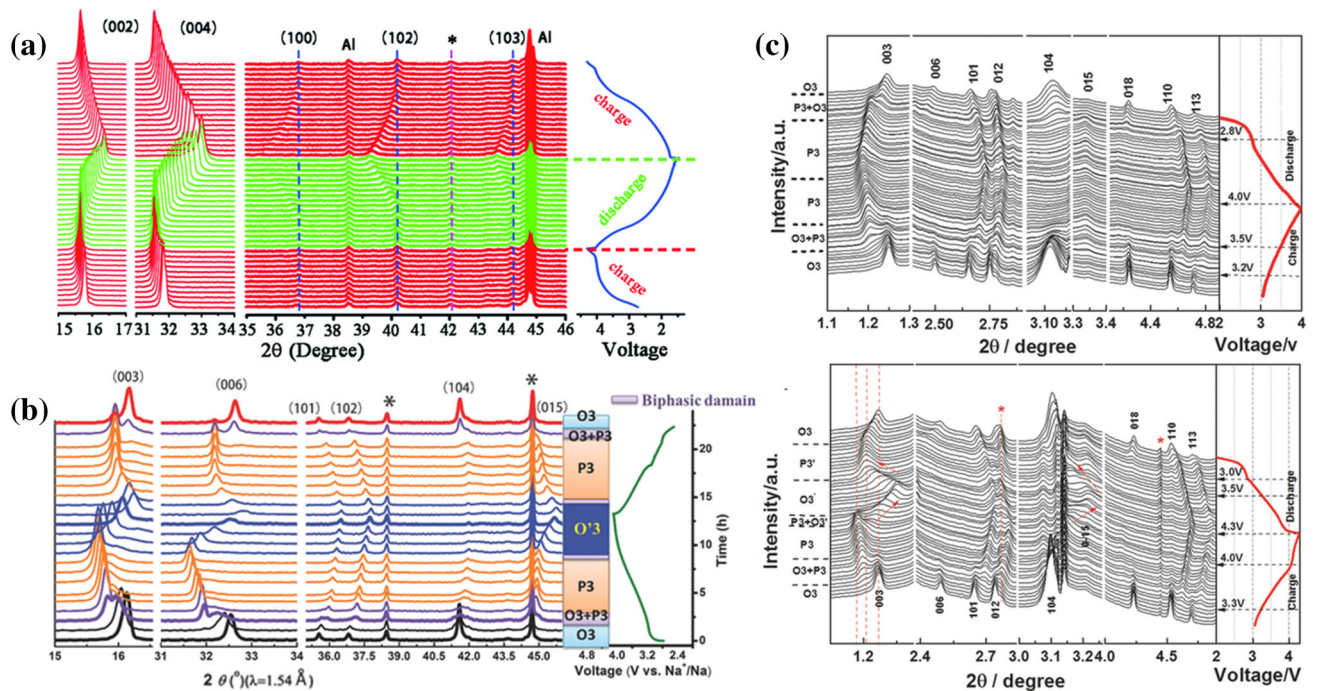

Figure 15 a In situ XRD patterns collected during the first charge/discharge and second charge of the P2-$Na_{0.67}Co_{0.5}Mn_{0.5}O_2$ electrode between 1.5 and 4.3 V. **b** In situ XRD patterns collected during the first charge/discharge process of the O3-layered metal oxide $Na_{0.9}[Cu_{0.22}Fe_{0.30}Mn_{0.48}]O_2$ electrode cycled between 2.5 and 4.1 V under a current rate of 0.1 C. **c** In situ XRD patterns collected during cycling of $Na_{1-\delta}Ni_{1/3}Fe_{1/3}Mn_{1/3}O_2$ electrode with different voltage ranges. **a** Reproduced with permission from Zhu et al. [124]. **b** Reproduced with permission from Mu et al. [125]. **c** Reproduced with permission from Xie et al. [14].

reaction process. With the help of inductively coupled plasma (ICP), the new phase is identified as $NaV_2(PO_4)_3$. The following discharge process just reverses the above process, and the calculated volume change from $Na_3V_2(PO_4)_3$ to $NaV_2(PO_4)_3$ is about 8.26%, verifying the excellent structural stability of $Na_3V_2(PO_4)_3$. Recently, Wang et al. [123] designed a novel $K_3V_2(PO_4)_3/C$ bundled nanowire and used it as the cathode material for SIBs for the first time. Similar to $NaV_2(PO_4)_3$, the compound $K_3V_2(PO_4)_3$ lattice also has a highly stable structure and fast ion diffusion. In the above work, further improvement obtained from constructing nanoporous structure and adding conductive carbon coating enhanced its capacity to 119 mA h g^{-1} at a current density of 100 mA g^{-1}. In situ XRD measurement of this material in Fig. 14b shows that only tiny shifts can be observed at two theta range of 23°–27° and 30°–34°, corresponding to a slight variation of the lattice parameters during the charge/discharge process.

Multi-layered compounds

Multi-layered oxides Na_xMO_2 (M = transition metals, one or more elements), with their high capacity, simple structure, and facile synthesis, have become one of the research focuses as the cathode materials in SIBs [26]. These compounds can be divided into two groups: P-type when Na^+ is stored in the prismatic site or O-type when Na^+ is stored in the octahedral site [10]. Zhu et al. [124] synthesized the P2-$Na_{0.67}$ $Co_{0.5}Mn_{0.5}O_2$ compound with a hierarchical architecture via a facile sol–gel method. This material delivered a very high discharge capacity of 147 mA h g^{-1} at the current rate of 0.1 C. *Via* in situ XRD technique, they determined the specific reaction route between 1.5 and 4.3 V versus Na^+/Na. According to Fig. 15a, during the whole process, only a solid-solution reaction has been observed. The (00 *l*) (*l* = 2 or 4) peaks shift to a lower angle upon charge, indicating the expansion along *c*-axis direction. This phenomenon is caused by the increased screening phenomenon of O^{2-}–O^{2-}. Besides, lattice parameters *a* and *b* show negligible change. Mu et al. [125] obtained an air-stable Co/Ni-Free O3-layered metal oxide $Na_{0.9}[Cu_{0.22}Fe_{0.30}Mn_{0.48}]O_2$ via a solid-state reaction. The related in situ XRD patterns revealed the reaction mechanism between 2.5 and 4.1 V very well, which is demonstrated in Fig. 15b. With

0.10–0.15 Na^+ de-intercalation, a two-phase reaction occurs with the coexistence of O3 and P3 phases [126]. Once O3 phase disappears, the P3 phase undergoes a solid-solution reaction until charged to 3.98 V. In the final charge process, the P3 phase transforms to a new hexagonal O3 phase. The next discharge process is a reversible process of the charge process. The diffraction patterns in Fig. 15c show that the reversible evolution of the O3–P3–P3–O3 hexagonal phase occurring in $Na_{1-\delta}Ni_{1/3}Fe_{1/3}Mn_{1/3}O_2$ depends on a cutoff voltage of 4.0 V, which was discovered by Xie et al. [14] When the cutoff voltage is raised to 4.3 V, two new monoclinic phases appeared. Correspondingly, the O3 phase is reversed via O3′–P3′–O3 transformation process.

The applications of in situ XRD have made great progress in the research of SIBs. Due to the active character of the sodium, strict sealing is required, which makes the in situ XRD characterization more difficult than that in LIBs, presenting a great challenge for in situ tests of SIBs.

Conclusions and perspective

It is clear that in situ XRD is a powerful method in probing reaction mechanisms in LIBs and SIBs. The useful information acquired from this method is important in the electrochemical process, such as volume change, crystal structure damage, and mechanical degradation. The obtained characterization results can explain the degradation mechanism and help building better batteries.

To acquire more useful information during electrochemical process, future development of in situ XRD should be focused on the improvement of detection precision and the combination with other advanced measurements, such as in situ TEM, in situ Raman, and ex situ devices like the temperature controller. For example, in situ XRD can be combined with the temperature controller to observe the performance of electrode materials under different temperatures, as well as the measurement of the enthalpy change of the electrochemical reactions. By using XRD refinement, the anisotropic temperature factors of each atom in the material can be calculated. With the observed thermal state, the vibration parameters of each atom can be determined. Moreover with the help of future analysis, this technique can give a more detailed information of the

electrochemical process with the help of future analysis. Other energy storage devices, such as lithium air and lithium sulfur batteries, involve the formation of lithium peroxide and the dissolution of polysulfide, which is hard to be detected via this method. In addition, for organic-based material, to achieve binder-free and low-angle detection is also a big challenge.

Acknowledgements

References

[1] Whittingham MS (2014) Ultimate limits to intercalation reactions for lithium batteries. Chem Rev 114:11414–11443. doi:10.1021/cr5003003

[2] Hu X, Zhang W, Liu X, Mei Y, Huang Y (2015) Nanostructured Mo-based electrode materials for electrochemical energy storage. Chem Soc Rev 44:2376–2404. doi:10.1039/c4cs00350k

[3] Islam MS, Fisher CA (2014) Lithium and sodium battery cathode materials: computational insights into voltage, diffusion and nanostructural properties. Chem Soc Rev 43:185–204. doi:10.1039/c3cs60199d

[4] Wang ZL, Xu D, Xu JJ, Zhang XB (2014) Oxygen electrocatalysts in metal-air batteries: from aqueous to nonaqueous electrolytes. Chem Soc Rev 43:7746–7786. doi:10.1039/c3cs60248f

[5] Palacin MR, de Guibert A (2016) Why do batteries fail? Science 351:1253292. doi:10.1126/science.1253292

[6] Tarascon JM, Vaughan G, Chabre Y et al (1999) In situ structural and electrochemical study of $Ni_{1-x}Co_xO_2$ metastable oxides prepared by soft chemistry. J Solid State Chem 147:410–420. doi:10.1006/jssc.1999.8465

[7] Palacín MR, Le Cras F, Seguin L et al (1999) In situ structural study of 4 V-range lithium extraction/insertion in fluorine-substituted $LiMn_2O_4$. J Solid State Chem 144:361–377. doi:10.1006/jssc.1999.8166

[8] Macklin WJ, Neat RJ, Sandhu SS (1992) Structural changes in vanadium oxide-based cathodes during cycling in a lithium polymer electrolyte cell. Electrochim Acta 37:1715–1720. doi:10.1016/0013-4686(92)80145-c

[9] Kumagai N, Kikuchi Y, Tanno K (1990) Kinetic and structural characteristics of niobium vanadium oxide electrodes for secondary lithium batteries. Solid State Ionics 40–41:978–981. doi:10.1016/0167-2738(90)90167-p

[10] Delmas C, Fouassier C, Hagenmuller P (1980) Structural classification and properties of the layered oxides. Phys B 99:81–85. doi:10.1016/0378-4363(80)90214-4

[11] Chung KY, Yoon WS, Lee HS et al (2006) In situ XRD studies of the structural changes of ZrO_2-coated $LiCoO_2$ during cycling and their effects on capacity retention in lithium batteries. J Power Sources 163:185–190. doi:10.1016/j.jpowsour.2005.12.063

[12] Shin HC, Bin Park S, Jang H et al (2008) Rate performance and structural change of Cr-doped $LiFePO_4$/C during cycling. Electrochim Acta 53:7946–7951. doi:10.1016/j.electacta.2008.06.005

[13] Yoon W-S, Nam K-W, Jang D et al (2012) The kinetic effect on structural behavior of mixed $LiMn_2O_4$–$LiNi_{1/3}Co_{1/3}Mn_{1/3}O_2$ cathode materials studied by in situ time-resolved X-ray diffraction technique. Electrochem Commun 15:74–77. doi:10.1016/j.elecom.2011.11.027

[14] Xie Y, Wang H, Xu G et al (2016) In operando XRD and TXM study on the metastable structure change of $NaNi_{1/3}Fe_{1/3}Mn_{1/3}O_2$ under electrochemical sodium-ion intercalation. Adv Energy Mater. doi:10.1002/aenm.201601306

[15] Ferguson TR, Bazant MZ (2014) Phase transformation dynamics in porous battery electrodes. Electrochim Acta 146:89–97. doi:10.1016/j.electacta.2014.08.083

[16] Lai W, Ciucci F (2010) Thermodynamics and kinetics of phase transformation in intercalation battery electrodes—phenomenological modeling. Electrochim Acta 56:531–542. doi:10.1016/j.electacta.2010.09.015

[17] Liu Y, Fujiwara T, Yukawa H, Morinaga M (2000) Lithium intercalation and alloying effects on electronic structures of spinel lithium manganese oxides. Sol Energy Mater Sol Cells 62:81–87. doi:10.1016/s0927-0248(99)00138-5

[18] Palacin MR (2009) Recent advances in rechargeable battery materials: a chemist's perspective. Chem Soc Rev 38:2565–2575. doi:10.1039/b820555h

[19] Chan CK, Peng H, Liu G et al (2008) High-performance lithium battery anodes using silicon nanowires. Nat Nanotechnol 3:31–35. doi:10.1038/nnano.2007.411

[20] Boukamp BA (1981) All-solid lithium electrodes with mixed-conductor matrix. J Electrochem Soc 128:725–729. doi:10.1149/1.2127495

[21] Hatchard TD, Dahn JR (2004) In situ XRD and electrochemical study of the reaction of lithium with amorphous silicon. J Electrochem Soc 151:A838–A842. doi:10.1149/1.1739217

[22] Obrovac MN, Christensen L (2004) Structural changes in silicon anodes during lithium insertion/extraction. Electrochem Solid State 7:A93–A96. doi:10.1149/1.1652421

[23] Li J, Dahn JR (2007) An in situ X-ray diffraction study of the reaction of Li with crystalline Si. J Electrochem Soc 154:A156–A161. doi:10.1149/1.2409862

[24] Misra S, Liu N, Nelson J, Hong SS, Cui Y, Toney MF (2012) In situ X-ray diffraction studies of (de)lithiation mechanism in silicon nanowire anodes. ACS Nano 6:5465–5473. doi:10.1021/nn301339g

[25] Baggetto L, Ganesh P, Sun CN, Meisner RA, Zawodzinski TA, Veith GM (2013) Intrinsic thermodynamic and kinetic properties of Sb electrodes for Li-ion and Na-ion batteries: experiment and theory. J Mater Chem A 1:7985–7994. doi:10.1039/c3ta11568b

[26] Kim SW, Seo DH, Ma XH, Ceder G, Kang K (2012) Electrode materials for rechargeable sodium-ion batteries: potential alternatives to current lithium-ion batteries. Adv Energy Mater 2:710–721. doi:10.1002/aenm.201200026

[27] Hewitt KC, Beaulieu LY, Dahn JR (2001) Electrochemistry of InSb as a Li insertion host problems and prospects. J Electrochem Soc 148:A402–A410. doi:10.1149/1.1359194

[28] Wang J (1986) Behavior of some binary lithium alloys as negative electrodes in organic solvent-based electrolytes. J Electrochem Soc 133:457–460. doi:10.1149/1.2108601

[29] Song JX, Zhou MJ, Yi R et al (2014) Interpenetrated gel polymer binder for high-performance silicon anodes in lithium-ion batteries. Adv Funct Mater 24:5904–5910. doi:10.1002/adfm.201401269

[30] Liu XH, Huang S, Picraux ST, Li J, Zhu T, Huang JY (2011) Reversible nanopore formation in Ge nanowires during lithiation-delithiation cycling: an in situ transmission electron microscopy study. Nano Lett 11:3991–3997. doi:10.1021/nl2024118

[31] Liu XH, Zheng H, Zhong L et al (2011) Anisotropic swelling and fracture of silicon nanowires during lithiation. Nano Lett 11:3312–3318. doi:10.1021/nl201684d

[32] Baggetto L, Notten PHL (2009) Lithium-ion (de)insertion reaction of germanium thin-film electrodes: an electrochemical and in situ XRD study. J Electrochem Soc 156:A169–A175. doi:10.1149/1.3055984

[33] Arico AS, Bruce P, Scrosati B, Tarascon JM, van Schalkwijk W (2005) Nanostructured materials for advanced energy conversion and storage devices. Nat Mater 4:366–377. doi:10.1038/nmat1368

[34] Etacheri V, Marom R, Elazari R, Salitra G, Aurbach D (2011) Challenges in the development of advanced Li-ion batteries: a review. Energy Environ Sci 4:3243–3262. doi:10.1039/c1ee01598b

[35] Wei W, Yang S, Zhou H, Lieberwirth I, Feng X, Mullen K (2013) 3D graphene foams cross-linked with pre-encapsulated Fe_3O_4 nanospheres for enhanced lithium storage. Adv Mater 25:2909–2914. doi:10.1002/adma.201300445

[36] Li L, Kovalchuk A, Fei HL et al (2015) Enhanced cycling stability of lithium-ion batteries using graphene-wrapped Fe_3O_4-graphene nanoribbons as anode materials. Adv Energy Mater 5:1500171. doi:10.1002/Aenm.201500171

[37] An Q, Lv F, Liu Q et al (2014) Amorphous vanadium oxide matrixes supporting hierarchical porous Fe_3O_4/graphene nanowires as a high-rate lithium storage anode. Nano Lett 14:6250–6256. doi:10.1021/nl5025694

[38] Balaya P, Li H, Kienle L, Maier J (2003) Fully reversible homogeneous and heterogeneous Li storage in RuO_2 with high capacity. Adv Funct Mater 13:621–625. doi:10.1002/adfm.200304406

[39] Delmer O, Balaya P, Kienle L, Maier J (2008) Enhanced potential of amorphous electrode materials: case study of RuO_2. Adv Mater 20:501–505. doi:10.1002/adma.200701349

[40] Gregorczyk KE, Kozen AC, Chen X et al (2015) Fabrication of 3D core-shell multiwalled carbon nanotube@RuO_2 lithium-ion battery electrodes through a RuO_2 atomic layer deposition process. ACS Nano 9:464–473. doi:10.1021/nn505644q

[41] Kim Y, Muhammad S, Kim H et al (2015) Probing the additional capacity and reaction mechanism of the RuO_2 anode in lithium rechargeable batteries. Chemsuschem 8:2378–2384. doi:10.1002/cssc.201403488

[42] Hassan AS, Moyer K, Ramachandran BR, Wick CD (2016) Comparison of storage mechanisms in RuO_2, SnO_2, and SnS_2 for lithium-ion battery anode materials. J Phys Chem C 120:2036–2046. doi:10.1021/acs.jpcc.5b09078

[43] Baudrin E (1999) Synthesis and electrochemical properties of cobalt vanadates vs. lithium. Solid State Ionics 123:139–153. doi:10.1016/s0167-2738(99)00096-x

[44] Wu F, Yu C, Liu W, Wang T, Feng J, Xiong S (2015) Large-scale synthesis of $Co_2V_2O_7$ hexagonal microplatelets under ambient conditions for highly reversible lithium storage. J Mater Chem A 3:16728–16736. doi:10.1039/c5ta03106k

[45] Luo Y, Xu X, Zhang Y et al (2016) Graphene oxide templated growth and superior lithium storage performance of novel hierarchical $Co_2V_2O_7$ nanosheets. ACS Appl Mater Interfaces 8:2812–2818. doi:10.1021/acsami.5b11510

[46] Wu ZS, Ren W, Wen L et al (2010) Graphene anchored with Co_3O_4 nanoparticles as anode of lithium ion batteries with enhanced reversible capacity and cyclic performance. ACS Nano 4:3187–3194. doi:10.1021/nn100740x

[47] Peng C, Chen B, Qin Y et al (2012) Facile ultrasonic synthesis of CoO quantum dot/graphene nanosheet composites with high lithium storage capacity. ACS Nano 6:1074–1081. doi:10.1021/nn202888d

[48] Yang G, Cui H, Yang G, Wang C (2014) Self-assembly of $Co_3V_2O_8$ multilayered nanosheets: controllable synthesis, excellent Li-storage properties, and investigation of electrochemical mechanism. ACS Nano 8:4474–4487. doi:10.1021/nn406449u

[49] Apostolova RD, Kolomoyets OV, Shembel' EM (2011) Optimization of iron sulfides usage in electrolytic composites with graphites for lithium-ion batteries. Surf Eng Appl Electrochem 47:465–470. doi:10.3103/s1068375511050036

[50] Balogun MS, Qiu W, Jian J et al (2015) Vanadium nitride nanowire supported SnS_2 nanosheets with high reversible capacity as anode material for lithium ion batteries. ACS Appl Mater Interfaces 7:23205–23215. doi:10.1021/acsami.5b07044

[51] Chung JS, Sohn HJ (2002) Electrochemical behaviors of CuS as a cathode material for lithium secondary batteries. J Power Sources 108:226–231. doi:10.1016/S0378-7753(02)00024-1

[52] Débart A, Dupont L, Patrice R, Tarascon JM (2006) Reactivity of transition metal (Co, Ni, Cu) sulphides versus lithium: the intriguing case of the copper sulphide. Solid State Sci 8:640–651. doi:10.1016/j.solidstatesciences.2006.01.013

[53] Tao HC, Yang XL, Zhang LL, Ni SB (2014) One-pot facile synthesis of CuS/graphene composite as anode materials for lithium ion batteries. J Phys Chem Solids 75:1205–1209. doi:10.1016/j.jpcs.2014.06.010

[54] Wang XX, Wang YH, Li X, Liu B, Zhao JB (2015) A facile synthesis of copper sulfides composite with lithium-storage properties. J Power Sources 281:185–191. doi:10.1016/j.jpowsour.2015.01.172

[55] Song T, Han H, Choi H et al (2015) TiO_2 nanotube branched tree on a carbon nanofiber nanostructure as an anode for high energy and power lithium ion batteries. Nano Res 7:491–501. doi:10.1007/s12274-014-0415-1

[56] Qiu J, Li S, Gray E et al (2014) Hydrogenation synthesis of blue TiO_2 for high-performance lithium-ion batteries. J Phys Chem C 118:8824–8830. doi:10.1021/jp501819p

[57] Wagemaker M, Borghols WJ, Mulder FM (2007) Large impact of particle size on insertion reactions. A case for anatase Li_xTiO_2. J Am Chem Soc 129:4323–4327. doi:10.1021/ja067733p

[58] Shen K, Chen H, Klaver F, Mulder FM, Wagemaker M (2014) Impact of particle size on the non-equilibrium phase transition of lithium-inserted anatase TiO_2. Chem Mater 26:1608–1615. doi:10.1021/cm4037346

[59] Li HQ, Liu XZ, Zhai TY, Li D, Zhou HS (2013) Li_3VO_4: a promising insertion anode material for lithium-ion batteries. Adv Energy Mater 3:428–432. doi:10.1002/aenm.201200833

[60] Liang ZY, Lin ZP, Zhao YM et al (2015) New understanding of Li_3VO_4/C as potential anode for Li-ion batteries: preparation, structure characterization and lithium insertion mechanism. J Power Sources 274:345–354. doi:10.1016/j.jpowsour.2014.10.024

[61] Li QD, Wei QL, Sheng JZ et al (2015) Mesoporous Li_3VO_4/C submicron-ellipsoids supported on reduced graphene oxide as practical anode for high-power lithium-ion batteries. Adv Sci 2:1500284. doi:10.1002/advs.201500284

[62] Zhou LL, Shen SY, Peng XX et al (2016) New insights into the structure changes and interface properties of Li_3VO_4 anode for lithium-ion batteries during the initial cycle by in situ techniques. ACS Appl Mater Interfaces 8:23739–23745. doi:10.1021/acsami.6b07811

[63] Débart A, Paterson AJ, Bao J, Bruce PG (2008) α-MnO_2 nanowires: a catalyst for the O2 electrode in rechargeable lithium batteries. Angew Chem 120:4597–4600. doi:10.1002/ange.200705648

[64] Li L, Nan C, Lu J, Peng Q, Li Y (2012) alpha-MnO_2 nanotubes: high surface area and enhanced lithium battery properties. Chem Commun (Camb) 48:6945–6947. doi:10.1039/c2cc32306k

[65] Yuan Y, Nie A, Odegard GM et al (2015) Asynchronous crystal cell expansion during lithiation of K^+-stabilized alpha-MnO_2. Nano Lett 15:2998–3007. doi:10.1021/nl5048913

[66] Chen WM, Qie L, Shao QG, Yuan LX, Zhang WX, Huang YH (2012) Controllable synthesis of hollow bipyramid beta-MnO_2 and its high electrochemical performance for lithium storage. ACS Appl Mater Interfaces 4:3047–3053. doi:10.1021/am300410z

[67] Chen R (1997) Cathodic behavior of alkali manganese oxides from permanganate. J Electrochem Soc 144:L64–L67. doi:10.1149/1.1837554

[68] Pang WK, Peterson VK, Sharma N, Zhang C, Guo Z (2014) Evidence of solid-solution reaction upon lithium insertion into cryptomelane $K_{0.25}Mn_2O_4$ material. J Phys Chem C 118:3976–3983. doi:10.1021/jp411687n

[69] Brezesinski T, Wang J, Tolbert SH, Dunn B (2010) Ordered mesoporous alpha-MoO$_3$ with iso-oriented nanocrystalline walls for thin-film pseudocapacitors. Nat Mater 9:146–151. doi:10.1038/nmat2612

[70] Lee SH, Kim YH, Deshpande R et al (2008) Reversible lithium-ion insertion in molybdenum oxide nanoparticles. Adv Mater 20:3627–3632. doi:10.1002/adma.200800999

[71] Zhou L, Yang L, Yuan P, Zou J, Wu Y, Yu C (2010) α-MoO$_3$ nanobelts: a high performance cathode material for lithium ion batteries. J Phys Chem C 114:21868–21872. doi:10.1021/jp108778v

[72] Ni JF, Wang GB, Yang J et al (2014) Carbon nanotube-wired and oxygen-deficient MoO$_3$ nanobelts with enhanced lithium-storage capability. J Power Sources 247:90–94. doi:10.1016/j.jpowsour.2013.08.068

[73] Wang X-J, Nesper R, Villevieille C, Novák P (2013) Ammonolyzed MoO$_3$ nanobelts as novel cathode material of rechargeable Li-ion batteries. Adv Energy Mater 3:606–614. doi:10.1002/aenm.201200692

[74] Mai LQ, Hu B, Chen W et al (2007) Lithiated MoO$_3$ nanobelts with greatly improved performance for lithium batteries. Adv Mater 19:3712–3716. doi:10.1002/adma.200700883

[75] Dong YF, Xu XM, Li S et al (2015) Inhibiting effect of Na$^+$ pre-intercalation in MoO$_3$ nanobelts with enhanced electrochemical performance. Nano Energy 15:145–152. doi:10.1016/j.nanoen.2015.04.015

[76] An Q, Wei Q, Zhang P et al (2015) Three-dimensional interconnected vanadium pentoxide nanonetwork cathode for high-rate long-life lithium batteries. Small 11:2654–2660. doi:10.1002/smll.201403358

[77] Ren W, Zheng Z, Luo Y et al (2015) An electrospun hierarchical LiV$_3$O$_8$ nanowire-in-network for high-rate and long-life lithium batteries. J Mater Chem A 3:19850–19856. doi:10.1039/c5ta04643b

[78] Tian XC, Xu X, He L et al (2014) Ultrathin pre-lithiated V$_6$O$_{13}$ nanosheet cathodes with enhanced electrical transport and cyclability. J Power Sources 255:235–241. doi:10.1016/j.jpowsour.2014.01.017

[79] Liu HM, Zhou HS, Chen LP, Tang ZF, Yang WS (2011) Electrochemical insertion/deinsertion of sodium on NaV$_6$O$_{15}$ nanorods as cathode material of rechargeable sodium-based batteries. J Power Sources 196:814–819. doi:10.1016/j.jpowsour.2010.07.062

[80] Wang H, Wang W, Ren Y, Huang K, Liu S (2012) A new cathode material Na$_2$V$_6$O$_{16}$·xH$_2$O nanowire for lithium ion battery. J Power Sources 199:263–269. doi:10.1016/j.jpowsour.2011.10.045

[81] Meng JS, Liu Z, Niu CJ et al (2016) A synergistic effect between layer surface configurations and K ions of potassium vanadate nanowires for enhanced energy storage performance. J Mater Chem A 4:4893–4899. doi:10.1039/c6ta00556j

[82] Niu C, Liu X, Meng J et al (2016) Three dimensional V$_2$O$_5$/NaV$_6$O$_{15}$ hierarchical heterostructures: controlled synthesis and synergistic effect investigated by in situ X-ray diffraction. Nano Energy 27:147–156. doi:10.1016/j.nanoen.2016.06.057

[83] Yan M, Zhao L, Zhao K et al (2016) The capturing of ionized oxygen in sodium vanadium oxide nanorods cathodes under operando conditions. Adv Funct Mater 26:6555–6562. doi:10.1002/adfm.201602134

[84] Jang DH (1996) Dissolution of spinel oxides and capacily losses in 4 V Li/Li$_x$Mn$_2$O$_4$ cells. J Electrochem Soc 143:2204–2211. doi:10.1149/1.1836981

[85] Chung KY, Kim KB (2002) Investigation of structural fatigue in spinel electrodes using in situ laser probe beam deflection technique. J Electrochem Soc 149:A79–A85. doi:10.1149/1.1426396

[86] Chung KY, Lee HS, Yoon W-S, McBreen J, Yang X-Q (2006) Studies of LiMn$_2$O$_4$ capacity fading at elevated temperature using in situ synchrotron x-ray diffraction. J Electrochem Soc 153:A774–A780. doi:10.1149/1.2172565

[87] Hirayama M, Ido H, Kim K et al (2010) Dynamic structural changes at LiMn$_2$O$_4$/electrolyte interface during lithium battery reaction. J Am Chem Soc 132:15268–15276. doi:10.1021/ja105389t

[88] Padhi AK (1997) Phospho-olivines as positive-electrode materials for rechargeable lithium batteries. J Electrochem Soc 144:1188–1194. doi:10.1149/1.1837571

[89] Roberts MR, Madsen A, Nicklin C et al (2014) Direct observation of active material concentration gradients and crystallinity breakdown in LiFePO$_4$ electrodes during charge/discharge cycling of lithium batteries. J Phys Chem C 118:6548–6557. doi:10.1021/jp411152s

[90] Villevieille C, Sasaki T, Novak P (2014) Novel electrochemical cell designed for operando techniques and impedance studies. RSC Adv 4:6782–6789. doi:10.1039/c3ra46184j

[91] Gibot P, Casas-Cabanas M, Laffont L et al (2008) Room-temperature single-phase Li insertion/extraction in nanoscale Li$_x$FePO$_4$. Nat Mater 7:741–747. doi:10.1038/nmat2245

[92] Delacourt C, Poizot P, Tarascon JM, Masquelier C (2005) The existence of a temperature-driven solid solution in Li$_x$FePO$_4$ for $0 \le x \le 1$. Nat Mater 4:254–260. doi:10.1038/nmat1335

[93] Malik R, Zhou F, Ceder G (2011) Kinetics of non-equilibrium lithium incorporation in LiFePO$_4$. Nat Mater 10:587–590. doi:10.1038/nmat3065

[94] Chen J, Graetz J (2011) Study of antisite defects in hydrothermally prepared LiFePO$_4$ by in situ X-ray diffraction. ACS Appl Mater Interfaces 3:1380–1384. doi:10.1021/am200141a

[95] Liu H, Strobridge FC, Borkiewicz OJ et al (2014) Capturing metastable structures during high-rate cycling of LiFePO$_4$ nanoparticle electrodes. Science 344:1252817. doi:10.1126/science.1252817

[96] Yan MY, Zhang GB, Wei QL et al (2016) In operando observation of temperature dependent phase evolution in lithium-incorporation olivine cathode. Nano Energy 22:406–413. doi:10.1016/j.nanoen.2016.01.031

[97] Chevrier VL, Ceder G (2011) Challenges for Na-ion negative electrodes. J Electrochem Soc 158:A1011–A1014. doi:10.1149/1.3607983

[98] Kim C, Lee KY, Kim I et al (2016) Long-term cycling stability of porous Sn anode for sodium-ion batteries. J Power Sources 317:153–158. doi:10.1016/j.jpowsour.2016.03.060

[99] Xu YH, Zhu YJ, Liu YH, Wang CS (2013) Electrochemical performance of porous carbon/tin composite anodes for sodium-ion and lithium-ion batteries. Adv Energy Mater 3:128–133. doi:10.1002/aenm.201200346

[100] Ellis LD, Hatchard TD, Obrovac MN (2012) Reversible insertion of sodium in tin. J Electrochem Soc 159:A1801–A1805. doi:10.1149/2.037211jes

[101] Yang D, Zheng Z, Liu H et al (2008) Layered titanate nanofibers as efficient adsorbents for removal of toxic radioactive and heavy metal ions from water. J Phys Chem C 112:16275–16280. doi:10.1021/jp803826g

[102] Izawa H, Kikkawa S, Koizumi M (1982) Ion exchange and dehydration of layered [sodium and potassium] titanates, Na$_2$Ti$_3$O$_7$ and K$_2$Ti$_4$O$_9$. J Phys Chem 86:5023–5026. doi:10.1021/j100222a036

[103] Senguttuvan P, Rousse G, Seznec V, Tarascon JM, Palacin MR (2011) Na$_2$Ti$_3$O$_7$: lowest voltage ever reported oxide insertion electrode for sodium ion batteries. Chem Mater 23:4109–4111. doi:10.1021/cm202076g

[104] Fu S, Ni J, Xu Y, Zhang Q, Li L (2016) Hydrogenation driven conductive Na$_2$Ti$_3$O$_7$ nanoarrays as robust binder-free anodes for sodium-ion batteries. Nano Lett 16:4544–4551. doi:10.1021/acs.nanolett.6b01805

[105] Ni J, Fu S, Wu C et al (2016) Superior sodium storage in Na$_2$Ti$_3$O$_7$ nanotube arrays through surface engineering. Adv Energy Mater 6:1502568. doi:10.1002/aenm.201502568

[106] Masquelier C, Croguennec L (2013) Polyanionic (phosphates, silicates, sulfates) frameworks as electrode materials for rechargeable Li (or Na) batteries. Chem Rev 113:6552–6591. doi:10.1021/cr3001862

[107] Yabuuchi N, Kubota K, Dahbi M, Komaba S (2014) Research development on sodium-ion batteries. Chem Rev 114:11636–11682. doi:10.1021/cr500192f

[108] Wu C, Kopold P, Ding YL, van Aken PA, Maier J, Yu Y (2015) Synthesizing porous NaTi$_2$(PO$_4$)$_3$ nanoparticles embedded in 3D graphene networks for high-rate and long cycle-life sodium electrodes. ACS Nano 9:6610–6618. doi:10.1021/acsnano.5b02787

[109] Jiang Y, Shi J, Wang M, Zeng L, Gu L, Yu Y (2016) Highly reversible and ultrafast sodium storage in NaTi$_2$(PO$_4$)$_3$ nanoparticles embedded in nanocarbon networks. ACS Appl Mater Interfaces 8:689–695. doi:10.1021/acsami.5b09811

[110] Xu C, Xu Y, Tang C et al (2016) Carbon-coated hierarchical NaTi$_2$(PO$_4$)$_3$ mesoporous microflowers with superior sodium storage performance. Nano Energy 28:224–231. doi:10.1016/j.nanoen.2016.08.026

[111] Chhowalla M, Shin HS, Eda G, Li LJ, Loh KP, Zhang H (2013) The chemistry of two-dimensional layered transition metal dichalcogenide nanosheets. Nat Chem 5:263–275. doi:10.1038/nchem.1589

[112] Bloise AC, Donoso JP, Magon CJ et al (2002) NMR study of lithium dynamics and molecular motions in a diethylamine-molybdenum disulfide intercalation compound. J Phys Chem B 106:11698–11707. doi:10.1021/jp012839m

[113] Wang X, Shen X, Wang Z, Yu R, Chen L (2014) Atomic-scale clarification of structural transition of MoS$_2$ upon sodium intercalation. ACS Nano 8:11394–11400. doi:10.1021/nn505501v

[114] Ou X, Xiong XH, Zheng FH et al (2016) In situ X-ray diffraction characterization of NbS$_2$ nanosheets as the anode material for sodium ion batteries. J Power Sources 325:410–416. doi:10.1016/j.jpowsour.2016.06.055

[115] Yang E, Ji H, Jung Y (2015) Two-dimensional transition metal dichalcogenide monolayers as promising sodium ion battery anodes. J Phys Chem C 119:26374–26380. doi:10.1021/acs.jpcc.5b09935

[116] Cao Y, Xiao L, Wang W et al (2011) Reversible sodium ion insertion in single crystalline manganese oxide nanowires with long cycle life. Adv Mater 23:3155–3160. doi:10.1002/adma.201100904

[117] Whitacre JF, Tevar A, Sharma S (2010) Na$_4$Mn$_9$O$_{18}$ as a positive electrode material for an aqueous electrolyte sodium-ion energy storage device. Electrochem Commun 12:463–466. doi:10.1016/j.elecom.2010.01.020

[118] Kim H, Kim DJ, Seo D-H et al (2012) Ab initio study of the sodium intercalation and intermediate phases in Na$_{0.44}$MnO$_2$ for sodium-ion battery. Chem Mater 24:1205–1211. doi:10.1021/cm300065y

[119] Sauvage F, Laffont L, Tarascon JM, Baudrin E (2007) Study of the insertion/deinsertion mechanism of sodium

into $Na_{0.44}MnO_2$. Inorg Chem 46:3289–3294. doi:10.1021/ic0700250

[120] Ren W, Zheng Z, Xu C et al (2016) Self-sacrificed synthesis of three-dimensional $Na_3V_2(PO_4)_3$ nanofiber network for high-rate sodium-ion full batteries. Nano Energy 25:145–153. doi:10.1016/j.nanoen.2016.03.018

[121] Xu Y, Wei Q, Xu C et al (2016) Layer-by-layer $Na_3V_2(PO_4)_3$ embedded in reduced graphene oxide as superior rate and ultralong-life sodium-ion battery cathode. Adv Energy Mater 6:1600389. doi:10.1002/aenm.201600389

[122] Jian Z, Han W, Lu X et al (2013) Superior electrochemical performance and storage mechanism of $Na_3V_2(PO_4)_3$ cathode for room-temperature sodium-ion batteries. Adv Energy Mater 3:156–160. doi:10.1002/aenm.201200558

[123] Wang XP, Niu CJ, Meng JS et al (2015) Novel $K_3V_2(PO_4)(_3)/C$ bundled nanowires as superior sodium-ion

battery electrode with ultrahigh cycling stability. Adv Energy Mater 5:1500716. doi:10.1002/aenm.201500716

[124] Zhu Y-E, Qi X, Chen X et al (2016) A P2-$Na_{0.67}Co_{0.5}Mn_{0.5}O_2$ cathode material with excellent rate capability and cycling stability for sodium ion batteries. J Mater Chem A 4:11103–11109. doi:10.1039/c6ta02845d

[125] Mu L, Xu S, Li Y et al (2015) Prototype sodium-ion batteries using an air-stable and Co/Ni-free O3-layered metal oxide cathode. Adv Mater 27:6928–6933. doi:10.1002/adma.201502449

[126] Li X, Wu D, Zhou Y-N, Liu L, Yang X-Q, Ceder G (2014) O3-type $Na(Mn_{0.25}Fe_{0.25}Co_{0.25}Ni_{0.25})O_2$: a quaternary layered cathode compound for rechargeable Na ion batteries. Electrochem Commun 49:51–54. doi:10.1016/j.elecom.2014.10.003